

1 **Markedly different impacts of primary emissions and secondary**
2 **aerosol formation on aerosol mixing states revealed by simultaneous**
3 **measurements of CCNC, V/HTDMA, and SP2**

4 Jiangchuan Tao^{1,8}, Biao Luo^{1,8}, Weiqi Xu³, Gang Zhao⁶, Hanbin Xu⁵, Biao Xue^{1,8}, Miaomiao Zhai^{1,8},
5 Wanyun Xu⁴, Huarong Zhao⁷, Sanxue Ren⁷, Guangsheng Zhou⁷, Li Liu^{2,*}, Ye Kuang^{1,8,*}, Yele Sun³

6 ¹ Institute for Environmental and Climate Research, Jinan University, Guangzhou, Guangdong, China

7 ² Key Laboratory of Regional Numerical Weather Prediction, Institute of Tropical and Marine
8 Meteorology, China Meteorological Administration, Guangzhou, China.

9 ³ State Key Laboratory of Atmospheric Boundary Layer Physics and Atmospheric Chemistry, Institute
10 of Atmospheric Physics, Chinese Academy of Sciences, Beijing, China.

11 ⁴ State Key Laboratory of Severe Weather, Key Laboratory for Atmospheric Chemistry, Institute of
12 Atmospheric Composition, Chinese Academy of Meteorological Sciences, Beijing, China

13 ⁵ Experimental Teaching Center, Sun Yat-Sen University, Guangzhou, China

14 ⁶ State Key Joint Laboratory of Environmental Simulation and Pollution Control, International Joint
15 Laboratory for Regional Pollution Control, Ministry of Education, College of Environmental Sciences
16 and Engineering, Peking University, Beijing 100871, China

17 ⁷ Hebei Gucheng Agricultural Meteorology National Observation and Research Station, Chinese
18 Academy of Meteorological Sciences, Beijing, 100081, China

19 ⁸ Guangdong-Hongkong-Macau Joint Laboratory of Collaborative Innovation for Environmental
20 Quality, Jinan University, Guangzhou, Guangdong, China

21 Correspondence: Ye Kuang (kuangye@jnu.edu.cn), Li Liu (liul@gd121.cn)

22

23 **Abstract**

24 The aerosol mixing state is a crucial physicochemical property that affects the optical properties
25 and cloud condensation nuclei (CCN) activity. Multiple techniques are commonly employed to
26 determine the aerosol mixing states for various applications, and comparisons between these
27 techniques provide insights into the variations in aerosol chemical and physical properties. These
28 techniques include size-resolved CCN activity measurements using a system with a CCN counter
29 (CCNC) coupled with a differential mobility analyzer (DMA), a Humidified/Volatility Tandem
30 Differential Mobility Analyzer (H/V-TDMA) that measures aerosol hygroscopicity and volatility
31 distributions, and a single-particle soot photometer (SP2) that directly quantifies black carbon (BC)
32 mixing states. This study provides the first comparison of aerosol mixing state parameters obtained
33 through simultaneous measurements using DMA-CCNC, H/VTDMA, and DMA-SP2. The impacts of
34 primary aerosol emissions and secondary aerosol (SA) formation on the aerosol mixing states and the
35 intercomparison results were analyzed. The results showed that the differences in the mixing-state
36 parameters measured using different techniques varied significantly under different conditions. The
37 V-TDMA and DMA-SP2 measurements showed that the non-volatile population identified by V-
38 TDMA was mainly contributed by the BC-containing aerosols. HTDMA and DMA-SP2
39 measurements indicated that a substantial proportion of nearly hydrophobic aerosols did not originate
40 from BC-containing aerosols but likely originated from fossil fuel combustion and biomass-burning
41 emissions. The synthesized comparison results between the DMA-CCNC, HTDMA, and DMA-SP2
42 measurements revealed that some nearly hydrophobic BC-free particles were CCN-inactive under
43 supersaturated conditions, likely from fossil fuel combustion emissions. In contrast, others were CCN-
44 active under supersaturated conditions linked to biomass-burning emissions. BC-containing aerosols
45 emitted from fossil fuel combustion tend to be more externally mixed with other aerosol components
46 than those emitted by biomass-burning activities. These results highlight significant disparities in the
47 mixing states and physiochemical properties of aerosols from fossil fuel and biomass burning. The
48 formation of secondary nitrate and organic aerosols significantly affects variations in aerosol mixing
49 states, generally enhancing aerosol hygroscopicity and volatility while reducing differences in mixing
50 state parameters derived from different techniques, reducing aerosol heterogeneity. Variations in the
51 number of BC-free particle fractions showed that SAs tended to form more quickly on BC-free

52 particles than on BC-containing particles. Further comparison of the mixing state parameters revealed
53 that the two resolved secondary organic aerosol factors in this study exhibited remarkably different
54 physical properties, indicating that they likely formed through different pathways. These findings
55 suggest that comparisons among aerosol mixing states derived from different techniques can provide
56 deeper insights into the physical properties of aerosols and how they are affected by SA formation,
57 aiding the investigation of SA formation pathways.

58 **1 Introduction**

59 The aerosol mixing state is a crucial physicochemical property of aerosol particles (Riemer et al.,
60 2019), exerting a significant impact on their optical properties and cloud condensation nuclei (CCN)
61 activity, thus affecting their impact on the climate and environment (Fierce et al., 2017; Riemer et al.,
62 2019; Stevens et al., 2022). For example, variations in the mixing state of black carbon (BC) particles
63 can significantly alter their absorption and radiative effects (Bond et al., 2013; Lack et al., 2012; Zhao
64 et al., 2019; Moffet et al., 2016; Matsui et al., 2018; Peng et al., 2016). Using simple internal mixing
65 state assumptions for aerosol chemical compositions to estimate CCN number concentrations can lead
66 to substantial overestimations (up to 30%; Deng et al., 2013; Farmer et al., 2015; Ren et al., 2018;
67 Ching et al., 2017, 2019; Tao et al., 2021). The aerosol mixing state varies widely due to complex
68 emissions and atmospheric transformations, leading to significant uncertainties in estimating the
69 effects of aerosols based on simplified mixing state assumptions (Ervens, 2015; Wang et al., 2022; Fu
70 et al., 2022).

71 The aerosol mixing state describes the mixture of aerosol chemical components within each
72 particle and the distribution of these particles in the aerosol population. This property can be directly
73 measured using single-particle chemical composition techniques (Fierce et al., 2017; Riemer et al.,
74 2019), such as the single-particle soot photometer (SP2), which measures refractory black carbon (rBC)
75 mass concentrations and the mixing state of rBC with other aerosol components, or single-particle
76 chemical composition measurement techniques (e.g., single-particle aerosol mass spectrometer, SP-
77 AMS) that have been developed in recent years (Lee et al., 2019; Riemer et al., 2019 and reference
78 therein). Alternatively, the aerosol mixing state can be inferred from indirect measurements of aerosol
79 properties, such as size-resolved aerosol CCN activity (measured by coupling a differential mobility
80 analyzer (DMA) and a CCN counter (CCNC)), size-resolved aerosol hygroscopicity distributions, or
81 volatility distributions (measured by a Humidified/Volatility Tandem differential mobility analyzer
82 (H/V-TDMA)).

83 However, each technique yields information on aerosol mixing states based on different aerosol
84 microphysical properties, thus obtaining aerosol mixing states that are different but linked to one
85 another. For instance, while both CCN activity and hygroscopic growth measurements are associated
86 with aerosol hygroscopicity, an intercomparison between CCNC and HTDMA measurements has

87 prompted investigations into aerosol hygroscopicity variations under different saturation conditions
88 (Su et al., 2010; Juranyi et al., 2013; Lance et al., 2013; Kawana et al., 2016; Tao et al., 2020; Jiang et
89 al., 2021). Although the SP2 and VTDMA techniques depend on the evaporation of non-refractory
90 compositions, only rBC remains in the SP2 measurements. In contrast, non-refractory composition
91 evaporation depends on the thermodynamic temperature in the VTDMA measurements. Thus,
92 measurements of an SP2 are highly correlated to those of a VTDMA at high temperatures (200 °C–
93 300 °C), with their differences reflecting variations in aerosol density, shape, or volatility (Philippin
94 et al., 2004; Wehner et al., 2009; Adachi et al., 2018, 2019; Wang et al., 2022). HTDMA and VTDMA
95 can be combined to study the influence of the aerosol mixing state on hygroscopicity and volatility
96 (Zhang et al., 2016; Cai et al., 2017; Wang et al., 2017). Strong correlations were found between the
97 hydrophobic and non-volatile particles, suggesting they might have similar chemical compositions
98 (Zhang et al., 2016). In addition, some studies have shown that, except for BC, low-volatility particles
99 correlate well with CCN-inactive particles based on VTDMA and CCNC measurements (Kuwata et
100 al., 2007; Kuwata and Kondo, 2008; Rose et al., 2011; Cheng et al., 2012). Therefore,
101 intercomparisons between mixing state parameters measured by distinct techniques provide a better
102 characterization of the aerosol mixing state and insight into aerosol physiochemical properties.
103 Previous studies have mainly compared two types of aerosol mixing state measurements and lacked a
104 comprehensive comparative analysis among SP2, DMA-CCN, and HV-TDMA measurements,
105 hindering the wide application of derived aerosol mixing states obtained by individual techniques.

106 The mixing state of primary aerosols can vary greatly depending on their type and emission
107 conditions (Cheng et al., 2012; Wang et al., 2017; Wang et al., 2022; Ting et al., 2018; Liu et al., 2021)
108 and can be significantly altered during aging processes or secondary formations (Wehner et al., 2009;
109 Cheng et al., 2012; Wang et al., 2022; Tomlin et al., 2021; Lata et al., 2021). Primary aerosol emissions,
110 such as biomass burning, fossil fuel combustion, and cooking, tend to contribute to weak
111 hygroscopicity (Herich et al., 2008, 2009; Wang et al., 2020; Kim et al., 2020) and low-volatility
112 aerosols (Hong et al., 2017; Saha et al., 2018). The formation of secondary aerosols (SAs), including
113 the aging of BC-containing aerosols and primary organic aerosols, mainly contributes to aerosols with
114 strong CCN activity (Mei et al., 2013; Ma et al., 2016; Tao et al., 2021) and high hygroscopicity (Chen
115 et al., 2018; Kim et al., 2020; Wang et al., 2020). It is important to study the impact of specific primary

116 aerosol emissions and SA formation on aerosol mixing states and the influence of aerosol mixing state
117 parameters derived from different techniques to enhance our understanding of the mixing state of
118 aerosols from different emission sources and improve their characterization in models.

119 The North China Plain (NCP) is among the most polluted regions in China, with various primary
120 emission sources and strong SA formations that play critical roles in air pollution (Xu et al., 2011; Tao
121 et al., 2012; Liu et al., 2015). The complex mixing state of aerosols in the NCP contributes to
122 uncertainties in evaluating their climate and environmental effects (Zhuang et al., 2013; Nordmann et
123 al., 2014; Zhang et al., 2016; Tao et al., 2020; Shi et al., 2022), particularly regarding BC particles
124 (Wu et al., 2017; Liu et al., 2019; Zhao et al., 2019; Wang et al., 2011; Zheng et al., 2019).
125 Meteorological conditions can greatly affect SA formation in the NCP and can be significantly
126 exacerbated during severe pollution events. SA formation under low relative humidity (RH) conditions,
127 mainly through the condensation of gaseous-phase oxidation products, would change to that mainly
128 occurring in the aqueous phase under high RH conditions (Kuang et al., 2020). Because SAs formed
129 through different mechanisms, have different chemical compositions and add mass to different aerosol
130 populations, SA formation under different meteorological conditions can affect the aerosol mixing
131 states differently (Tao et al., 2021). This study obtained the aerosol mixing state through concurrent
132 measurements of the CCN activity, hygroscopicity, volatility, and BC particles at a regional site in the
133 NCP using CCNC, HTDMA, VTDMA, and SP2 instruments. This provides a unique opportunity to
134 perform a comprehensive inter-comparison of the aerosol mixing states among different techniques to
135 gain insight into the impact of primary aerosol emissions and SA formation on the observed aerosol
136 mixing states.

137

138 **2 Materials and methods**

139 **2.1 Campaign information and instruments setup**

140 From the 16th of October to the 16th of November 2021, aerosol mixing states were continuously
141 and concurrently monitored using different techniques at the Gucheng site in Dingxing County, Hebei
142 Province, China, as part of a campaign to investigate AQueous Secondary aerosol formation in fog
143 and aerosols and their radiative effects in the NCP (AQ-SOFAR). The observation site, located at
144 39°09'N, 115°44'E, is an Ecological and Agricultural Meteorology Station of the Chinese Academy

145 of Meteorological Sciences, situated between the megacities of Beijing (approximately 100 km away)
146 and Baoding (approximately 40 km away) and surrounded by farmlands and small towns. This site
147 provides a representative view of the background atmospheric pollution conditions in the NCP (Kuang
148 et al., 2020; Li et al., 2021).

149 Different measurement techniques were used to simultaneously obtain the aerosol mixing state
150 through CCN activity, hygroscopicity, volatility, and BC particle observations. In addition to aerosol
151 mixing state measurements, the AQ-SOFAR campaign includes measurements of aerosol number size
152 distribution, chemical composition, aerosol scattering, and absorption properties. Aerosol number size
153 distributions in the diameter range of 13 nm–4 μm were measured by the scanning mobility particle
154 sizer (13–550 nm) and the aerodynamic aerosol classifier (100 nm–4 μm), and they are merged by
155 assuming an aerosol density of 1.6 g/cm^3 . The total BC mass concentrations were determined using an
156 aethalometer (Magee, AE33; Drinovec et al., 2015); more information on the correction of absorption
157 measurements and mass concentration calculations is available in Luo et al. (2022). All aerosol
158 measurement instruments were housed in a temperature-controlled container at 24 $^{\circ}\text{C}$. The inlet was
159 switched among three impactors: TSP (Total Suspended Particles), $\text{PM}_{2.5}$ (Particulate Matter with an
160 aerodynamic diameter of less than 2.5 μm), and PM_1 (Particulate Matter with an aerodynamic diameter
161 of less than 1 μm). Inlet changes among impactors affect dry-state aerosol sampling owing to ambient
162 aerosols are enlarged through aerosol hygroscopic growth or activation. However, the aerosol mixing
163 state and aerosol chemical composition measurements were made on submicron aerosols, and the inlet
164 change almost did not affect those measurements under conditions of RH less than 90%. The sampled
165 aerosol was dried by two parallelly assembled Nafion dryers with a length of 1.2 m. Two Nafion driers
166 was used because of the high RH and sample flow rate ($\sim 16 \text{ L}/\text{min}$) during the campaign to ensure
167 drying efficiency. In addition, during autumn and winter in the NCP, ambient air temperature ($<20 \text{ }^{\circ}\text{C}$
168 and sometimes $<0 \text{ }^{\circ}\text{C}$) can be significantly lower than the room temperature ($\sim 24 \text{ }^{\circ}\text{C}$). Therefore, this
169 dryer system can maintain the RH of sampled aerosols to below 20%. Meteorological data such as
170 temperature, pressure, wind speed, wind direction, and RH were obtained from an automatic weather
171 station operated by the station.

172 The chemical composition of the submicron aerosols was analyzed using a High-Resolution
173 Time-of-Flight Aerosol Mass Spectrometer (HR-ToF-AMS). The ionization efficiency (IE) was
174 calibrated using 300 nm diameter pure NH_4NO_3 particles, following the standard protocols outlined in

175 Jayne et al. (2000) in the middle of the campaign, with the relative ionization efficiency (RIE) of
176 ammonium determined to be 5.26. The RIE of sulfate was 1.28 using pure $(\text{NH}_4)_2\text{SO}_4$ particles, and
177 the default RIEs of 1.4 for organic aerosols, 1.1 for nitrates, and 1.3 for chlorides were used as the
178 organic aerosols. The composition-dependent collection efficiency reported by Middlebrook et al.
179 (2012) was used. Elemental ratios were derived using the “Improved-Ambient (I-A)” method as
180 described in Canagaratna et al. (2015), including hydrogen to carbon (H/C), oxygen to carbon (O/C),
181 and organic mass to organic carbon (OM/OC) ratios. Two primary organic aerosol (POA) and two
182 oxygenated organic aerosol (OOA) factors were identified by High-Resolution Positive Matrix
183 Factorization (HR-PMF; Ulbrich et al., 2009; Paatero and Tapper, 1994). This study used the
184 summation of the two OOA factors to represent secondary organic aerosols (SOA). The mass spectra
185 of the organic aerosol (OA) factors and their correlations with external species are shown in Figs. S1
186 and S2. The Biomass Burning Organic Aerosol (BBOA) spectrum was characterized by obvious m/z
187 60 (mainly $\text{C}_2\text{H}_4\text{O}_2^+$) and 73 (mainly $\text{C}_3\text{H}_5\text{O}_2^+$), two indicators of biomass burning (Mohr et al., 2009).
188 BBOA correlated well with $\text{C}_2\text{H}_4\text{O}_2^+$ ($R^2=0.91$) and $\text{C}_3\text{H}_5\text{O}_2^+$ ($R^2=0.90$). Consistent with previous
189 studies in Beijing (Xu et al., 2019), the PMF analysis revealed a mixed factor named Fossil Fuel
190 Organic Aerosol (FFOA), which comprises traffic emissions and coal combustion and is characterized
191 by a typical hydrocarbon ion series. FFOA had a relatively high f_{44} (0.083) value, which was likely
192 due to aging during regional transportation, similar to the results observed in the winter of 2016 in
193 Beijing (Xu et al., 2019) and coal combustion organic aerosols in Gucheng (Chen et al., 2022).
194 Secondary organic aerosol formation from volatile organic compound precursors could occur in
195 different formation pathways, such as aqueous-phase, heterogeneous, or gas-phase reactions. It might
196 also be oxidized under different conditions, such as oxidation under different nitrogen oxide conditions
197 with different oxidation capacities and oxidants. The two resolved OOA factors displayed different
198 spectral patterns, correlations with tracers, and diurnal variations, suggesting that they resulted from
199 different chemical processes. However, their formation mechanisms remain to be explored in future
200 studies. In general, the OOA factor 1 (OOA1) has higher $\text{CO}_2^+/\text{C}_2\text{H}_3\text{O}^+$ (3.9) and O/C (0.91) ratios
201 than OOA factor 2 (OOA2) with 2.1 and 0.78, respectively.

202 This study did not consider losses in the inlet line and sampling systems for the following
203 reasons: (1) investigated mixing state parameters are represented by number fractions (NFs) of

204 different diameters, which are much less affected by losses in sampling systems compared with
205 absolute number concentrations; and (2) good consistency was achieved between measurements of
206 particle number size distributions (PNSD) and mass concentrations measured by AMS. The average
207 ratio between volume concentration derived from AMS and rBC measurements (densities of
208 compounds are the same as Kuang et al., 2021) and the volume concentration derived from PNSD
209 measurements was 0.79 ($R=0.97$, as shown in Fig. S3), consistent with previous reports as AMS cannot
210 detect aerosol components, such as dust (Kuang et al., 2021).

211 **2.2 Aerosol mixing states measurement techniques**

212 **2.2.1 DMA-CCNC measurements**

213 The CCN activity of the particles under supersaturated conditions was measured using a DMA-
214 CCNC system, which consisted of a differential mobility analyzer (DMA; model 3081, TSI, Inc., MN,
215 USA), condensation particle counter (CPC; model 3756, TSI, Inc., MN, USA), and continuous-flow
216 CCNC (model CCN100, Droplet Measurement Technologies, USA). The system was operated in size-
217 scanning mode and provided the Size-resolved Particle Activation Ratio (SPAR) by combining CPC
218 and CCNC measurements at different particle sizes. To compare the instruments, three
219 supersaturations (SSs) of 0.08%, 0.14%, and 0.22% were applied in a single cycle of approximately
220 15 min. CCN measurements under these three SSs revealed that the CCN activity of aerosols resides
221 in the accumulation mode with an aerosol diameter range of approximately 100–200 nm, which is
222 close to the diameters of the HV-TDMA measurements. Higher SSs would reveal CCN activities of
223 smaller aerosol particles (<100 nm), where the DMA-SP2 measurement is unavailable. The sample
224 and sheath flow rates of DMA were set at 1 and 5 lpm, respectively, resulting in a measured particle
225 diameter range of 9–500 nm, with a running time of 5 min per cycle. Supersaturation in the CCNC
226 was calibrated with monodisperse ammonium sulfate particles (Rose et al., 2008) before and after the
227 campaign. The flow rates were also calibrated before and after the campaign and checked daily to
228 minimize uncertainties in droplet counting and supersaturation formed in the column (Roberts and
229 Nenes, 2005; Lance et al., 2006). SPAR deviations due to multiple-charge particles were corrected
230 using a modified algorithm based on Hagen and Alofs (1983) and Deng et al. (2011). Further details
231 regarding this system can be found in Ma et al. (2016) and Tao et al. (2021).

232 **2.2.2 H/V-TDMA measurements**

233 The mixing state of the aerosols in terms of hygroscopicity and volatility was measured using a
234 Hygroscopicity/Volatility Tandem Differential Mobility Analyzer (H/V-TDMA; Tan et al., 2013). The
235 H/V-TDMA consisted of two DMA (Model 3081 L, TSI Inc.), with the first DMA (DMA1) selecting
236 dried particles without conditioning (RH ~15%) and the second DMA (DMA2) selecting conditioned
237 particles. H/V-TDMA can operate in either H- or V-mode, controlled by a three-way solenoid valve.
238 A Nafion humidifier was used in the H-mode to condition the selected dry particles to 90% RH
239 equilibrium. The number-size distribution of humidified particles (D_p) was measured using DMA2 and
240 CPC (Model 3772, TSI Inc.). The RH-dependent hygroscopic growth factor (GF) at a specific diameter
241 (D_d) was calculated as follows:

$$242 \quad GF = \frac{D_p(RH)}{D_d} \quad (1)$$

243 where $D_p(RH)$ is the size of particles undergoing humidification. Four dry electrical mobility diameters
244 (50, 100, 150, and 200 nm) were measured in this mode. The instrument was regularly calibrated using
245 standard polystyrene latex spheres (PSL) and ammonium sulfate particles.

246 In V-mode, a heated tube evaporated the volatile coatings from the previously selected dry
247 particles. Six temperature settings were used for the heated tube, ranging from 25–200°C. The number-
248 size distributions of the heated particles were measured using DMA2 and CPC. In addition to the four
249 particle sizes measured in the H-mode, three additional particle sizes (250, 300, and 350 nm) were
250 measured in the V-mode (residence time inside the heated tube to be about 1.6 s; Hong et al., 2017).
251 The temperature-dependent shrinkage factor (SF), which is the ratio of heated particle size to dry
252 particle size without heating (D_d), is defined as:

$$253 \quad SF = \frac{D_p(T)}{D_d} \quad (2)$$

254 where $D_p(T)$ denotes the particle diameter during heating. A complete cycle of H-mode
255 measurements under one RH condition and V-mode measurements at six temperatures took
256 approximately 3 h. The Probability Density Function (PDF) of the GF (or SF) was calculated from the
257 measured density function using the inversion algorithm described by Stolzenburg and McMurry
258 (2008).

259 **2.2.3 DMA-SP2 measurements**

260 The size-resolved BC mixing states were measured using an SP2 (Droplet Measurement
261 Technology, Inc., USA) after DMA (Model 3081, TSI, USA). The DMA selected aerosols of various
262 dry particle sizes, which were then introduced into SP2. The DMA-SP2 setup was able to measure the
263 mixing states of aerosols with diameters (detection limit of approximately 80 nm based on the
264 calibration) of 100, 120, 160, 200, 235, 270, 300, 335, 370, 400, 435, 470, 500, 535, 570, 600, 635,
265 670, and 700 nm within 20 min when it was not placed after an enuder-bypass switch system (the 13th
266 to the 24th of October, 09:00 am of the 5th of November to 09:00 am of the 8th of November). However,
267 it only measured mixing states at diameters of 120, 160, 200, 250, 300, 400, and 500 nm when it was
268 placed after a thermodenuder-bypass switch system (11:00 am of the 24th of October to 08:00 am of
269 the 5th of November, and 09:00 am of the 8th of November to 06:00 pm of the 17th of November).
270 Because the HTDMA and VTDMA measurements were conducted solely by a single H/VTDMA
271 system operating in different modes, the time needed for a single particle size measurement of
272 HTDMA and VTDMA was much longer than that of the DMA-SP2 system. Thus, more particle sizes
273 were selected in the DMA-SP2 system for acquiring the BC mass concentration and mixing state at
274 larger diameters than HTDMA and VTDMA.

275 The SP2 chamber had a continuous Nd:YAG laser beam with a wavelength of 1064 nm. The BC-
276 containing particles passing through the laser beam became incandescent by absorbing radiation. The
277 mass concentration of the BC was calculated by measuring the intensity of the emitted incandescent
278 light. The sheath flow/sample flow ratio was maintained at 10 for the DMA to reduce the width of the
279 diameter distribution of the selected monodisperse aerosols. Additionally, the flow rate of the SP2 was
280 changed from 0.1 to 0.12 L/min starting on the 22nd of October (allowed flow rate range of SP2: 0.03–
281 0.18 L/min from the specification). SP2 was calibrated using quadrag soot particles, as reported by
282 Gysel et al. (2011). Further details regarding the calibrations are provided in Section 1 of the
283 Supplementary Information.

284 **2.3 Derivations of mixing state parameters**

285 **2.3.1 Fitting SPAR curves measured by the DMA-CCNC system**

286 The SPAR curves were parameterized using a sigmoidal function with three parameters. As
287 shown in Fig. S4, a sigmoidal curve generally characterized the measured SPAR. This
288 parameterization assumes that the aerosol is an external mixture of CCN-active hydrophilic and CCN-

289 inactive hydrophobic particles (Rose et al., 2010). The formula used to parameterize the SPAR ($R_a(D_d)$)
290 for a specific SS is as follows (Rose et al., 2008):

$$291 \quad R_a(D_d) = \frac{\text{MAF}}{2} \left(1 + \operatorname{erf} \left(\frac{D_d - D_a}{\sqrt{2}\pi\sigma} \right) \right) \quad (7)$$

292 where erf denotes the error function. The Maximum Activation Fraction (MAF) is an asymptote of the
293 measured SPAR curve for large particles, as shown in Fig. S4, representing the fraction of CCNs
294 relative to the total number of particles. D_a is the midpoint activation diameter, is linked to the
295 hygroscopicity of the CCNs, and indicates the diameter where the SPAR equals half of the MAF value.
296 The σ is the standard deviation of the cumulative Gaussian distribution function and characterizes the
297 heterogeneity of CCN hygroscopicity. In Fig. S4, the σ indicates the slope of the steep increase in the
298 SPAR curves when the diameter is close to D_a . Generally, hydrophilic particles larger than D_a can
299 become CCN. Therefore, these three parameters can be used to characterize the hygroscopicity of these
300 hydrophilic particles. This study did not consider the impact of nearly hydrophobic particles on SPAR,
301 as deviations from this parameterization scheme due to this impact were negligible at low SSs, as
302 stated in Tao et al. (2020).

303

304 **2.3.2 Classification of particle type based on hygroscopicity or volatility**

305 In this study, ambient aerosol particles were classified into two groups based on their
306 hygroscopicity (hydrophobic and hydrophilic) and two groups based on their volatility (non-volatile
307 and volatile) based on the measurements from H/V-TDMA (Wehner et al., 2009; Liu et al., 2011;
308 Zhang et al., 2016). Each group can be defined using the critical values of GF or SF as follows:
309 hydrophobic population: $\text{GF} < \text{GF}_C$; hydrophilic population: $\text{GF} \geq \text{GF}_C$; non-volatile population: $\text{SF} \geq \text{SF}_C$;
310 and volatile population: $\text{SF} < \text{SF}_C$.

311 The critical values of GF (GF_C) and SF (SF_C) in H/V-TDMA depend on the particle size and
312 working conditions, such as relative humidity and heating temperature. During this campaign, the SF_C
313 was set to 0.85 for all seven measured particle sizes at a temperature of 200 °C. The GF_C for the four
314 measured particle sizes of 50, 100, 150, and 200 nm were 1.1, 1.15, 1.175, and 1.2, respectively, and
315 the corresponding hygroscopicity parameter, κ , was approximately 0.07. These values of GF_C and SF_C
316 divide the probability density functions (PDFs) of SF and GF into two modes, consistent with prior

317 NCP studies (Liu et al., 2011; Zhang et al., 2016). The NF for the hydrophilic group (NF_H) and volatile
318 group (NF_V) can be calculated as follows:

$$319 \quad \text{NF}_H = \int_{\text{GF}_C}^{\infty} \text{GFPDF}(GF) dGF \quad (7)$$

$$320 \quad \text{NF}_V = \int_0^{\text{SF}_C} \text{SFPDF}(SF) dSF \quad (8)$$

321 where GFPDF and SFPDF are the PDFs of GF and SF, respectively, derived from H/V-TDMA
322 measurements.

323 **2.3.3 Classification of particle type based on DMA-SP2 measurements**

324 BC-containing aerosols can be categorized into two groups based on coating thickness: bare
325 BC/thinly coated BC particles and thickly coated BC particles. For the measurement of coated BC
326 particles at SP2, the incandescence signal is generally detected later than the scattering signals and the
327 time difference between the occurrence of the peaks of the incandescence and scattering signals is
328 defined as the lag time (Moteki & Kondo, 2007; Sedlacek et al., 2012; Subramanian et al., 2010). The
329 coating thickness of BC-containing aerosols in the SP2 measurement can be indicated by the lag time
330 (Moteki and Kondo, 2007; Schwarz et al., 2006; Sedlacek et al., 2012; Subramanian et al., 2010;
331 Metcalf et al., 2012), which has exhibited a clear two-mode distribution in previous studies (Zhang et
332 al., 2018; Zhao et al., 2021). A critical lag time threshold can be used to differentiate between the
333 different types of BC-containing aerosols and calculate the NF of bare and coated BC particles in the
334 total identified aerosols. In this study, a two-mode distribution of the lag time (Δt) was observed, and
335 a critical value of 0.8 μs was used to classify the BC-containing particles into thinly coated (or bare)
336 BC ($\Delta t < 0.8 \mu\text{s}$) and thickly coated BC ($\Delta t \geq 0.8 \mu\text{s}$). The definitions of all abbreviations are listed in
337 Table 1.

338 **3 Results and discussions**

339 **3.1 Campaign overview**

340 The time series of the meteorological parameters, aerosol mixing state measurements using
341 different techniques, and mass concentrations of the aerosol chemical compositions are shown in Fig.
342 1. In detail, the measurements of aerosol mixing states include SPAR at an SS of 0.08% by DMA-

343 CCNC, GF-PDF (PDF of GF) at 200 nm by HTDMA, SF-PDF (PDF of SF) at 200 nm and 200 °C by
344 VTDMA, and lag time PDF of 200 nm BC-containing particles by DMA-SP2. The SIA, SOA, POA,
345 and BC mass concentrations are shown in Fig. 1 (b) . Three periods with significantly different aerosol
346 pollution conditions were identified during the campaign. As shown in Fig. 1(b), before the 23rd of
347 October (moderately polluted period), the accumulation of aerosols led to SIA mass concentrations
348 $<20 \mu\text{g}/\text{m}^3$. In contrast, the highest mass concentrations of SOA, POA, and BC reached beyond
349 $10 \mu\text{g}/\text{m}^3$. The mass concentrations of different aerosol components increased significantly from the
350 23rd of October to the 6th of November (heavily polluted period with an average non-refractory PM_{10}
351 mass concentration of $49.5 \pm 22.5 \mu\text{g}/\text{m}^3$) and decreased to much lower levels after the 6th of
352 November (clean period with a non-refractory PM_{10} mass concentration of $5.1 \pm 3.3 \mu\text{g}/\text{m}^3$). Two
353 particle groups were identified concerning the CCN activity, hygroscopicity, volatility, and coating
354 thickness, as demonstrated by the SPAR, GF-PDF, SF-PDF, and lag-time PDF of BC-containing
355 particles. Significant variations in the aerosol mixing states were also observed during the three periods
356 with different pollution conditions, as demonstrated by the variations in SF-PDF measured by
357 VTDMA. For example, the SF of the non-volatile particle group decreased during the heavily polluted
358 period. Aerosol mixing states may have changed because of various transformations in existing aerosol
359 particles and distinct secondary formation processes under different pollution conditions (Kuang et al.,
360 2020; Tao et al., 2021; Shi et al., 2022; Yang et al., 2022). Diurnal variations in the mass concentrations
361 of different aerosol chemical components and mixing states can be observed in the variations in the
362 SPAR measurements, as previously observed in this region (Liu et al., 2011; Ma et al., 2012; Kuang
363 et al., 2015; Tao et al., 2020).

364 Fig. 2 shows the campaign-averaged SPAR at the three SSs, PDF of the lag time of BC-containing
365 particles, GFPDF, and SFPDF at 200 °C for different particle sizes. The sigmoidal SPAR curves were
366 characterized by a rapid increase, followed by a gradual increase to unit 1, similar to the measured
367 SPAR curves previously observed in this region (Deng et al., 2011; Zhang et al., 2014; Ma et al., 2016;
368 Tao et al., 2018). At lower SSs, the particle size required for CCN activation was larger; thus, rapid
369 increases in the SPAR curves occurred at larger particle sizes. In addition, the maximum AR of the
370 SPAR curves decreases as fewer particles are CCN-active under low SSs. For the three measured SSs,
371 the particle sizes where SPAR equals approximately 0.5 are approximately 90, 120, and 180 nm for

372 the three SSs of 0.08%, 0.14%, and 0.22%, respectively, consistent with the average D_a (see Eq. 7)
373 values of the campaign. The NF of CCN-active particles in large-diameter ranges (which varies with
374 SS and, for example, is greater than 200 nm for 0.08%) can be indicated by the gradual increase in the
375 SPAR curves and quantified by the fitting parameter, MAF (see Eq. 7). The PDFs of the lag time, GF,
376 and SF were all characterized by a bimodal distribution, which indicates two particle groups of BC-
377 containing aerosols with different coating thicknesses, hygroscopicity, and volatility. The variations
378 in the aerosol mixing states were further analyzed based on the measured mixing state parameters.

379 **3.2 Intercomparisons among aerosol mixing state parameters derived using four techniques**

380 The size-dependent characteristics of the aerosol mixing state parameters derived from the
381 measurements of the four techniques and the MFs of different aerosol chemical compositions during
382 the three pollution periods are shown in Fig. 3. In general, the size-dependent characteristics of MAF,
383 NF_H , NF_V , and NF_{noBC} were similar, suggesting that they were likely dominated by the same particle
384 group, namely BC-free particles. This particle group had the highest fraction (>0.7) during the heavily
385 polluted period and the lowest fraction (down to 0.5) during the clean period, with the fraction
386 decreasing with increasing particle size. This suggests that primary emissions tend to have higher
387 fractions of BC-containing particles in larger diameter ranges; for example, the fraction of BC-
388 containing particles increases from ~ 0.1 to ~ 0.4 as the particle size increases from 200 to 500 nm
389 during the cleaning period. Because the bulk aerosol MF is mostly contributed by particles >300 nm,
390 there may have been more hydrophilic, volatile, CCN-active, and BC-free particles with larger sizes
391 (>300 nm) during the heavily polluted period owing to strong SA formation in larger diameter ranges
392 (Kuang et al., 2020), resulting in a higher NF of these particles compared to the clean period. As for
393 R_{exBC} , the small size dependence of R_{exBC} during the moderately polluted period might have been
394 associated with stronger primary emissions, while the decrease in R_{exBC} with increasing particle
395 diameter in the polluted period confirmed that SA formation is more efficient for particles with larger
396 diameters.

397 As for the difference among the aerosol mixing state parameters, NF_V and NF_{noBC} agreed with
398 each other with a <0.1 difference, and both were higher than NF_H by at least 0.1 NF_H in the moderately
399 polluted period. Compared with NF_{noBC} , NF_V was higher during the heavily polluted period, when the
400 nitrate fraction was the highest ($\sim 30\%$). The SOA fraction was the lowest ($\sim 7\%$) among all three

401 periods, suggesting that some BC-containing aerosols in this period were also identified as volatile,
402 consistent with the fact that the formation of semi-volatile nitrate in BC-containing particles increases
403 their volatility. However, during the cleaning period, NF_V was even lower than NF_{noBC} , suggesting that
404 some BC-free aerosols were characterized as low volatile and non-negligible fractions of BC-free
405 aerosols dominated these less volatile aerosol components, which were likely less volatile organic
406 aerosols (not likely contributed by BC-containing particles with a BC smaller than the SP2 detection
407 limit, because the SF of this type of volatile BC-containing aerosols has an SF lower than 80/200,
408 which is substantially lower than the threshold SF of 0.85 for NF_V calculation). In addition, the MAF
409 values generally agreed with the NF_H during the clean period. However, they were larger than the NF_H
410 during the moderately and heavily polluted periods (by ~ 0.2) when the POA/SOA fractions were
411 higher ($\sim 40\%$ vs. $\sim 35\%$). POA generally has a lower hygroscopicity than SOA. The critical κ of
412 hydrophilic mode aerosols was 0.07, suggesting that a higher fraction of aerosols had κ below 0.07
413 (i.e., hydrophobic mode aerosols in this study) during the moderately polluted period. However, under
414 supersaturated conditions, they demonstrate enhanced hygroscopicity by becoming CCN-active. NF_H
415 was consistently lower than NF_V and NF_{noBC} (the average difference between NF_H and NF_{noBC} was
416 approximately 0.2). As mentioned above, NF_H was also lower than MAF during moderately polluted
417 periods, and there may be a significant fraction of volatile BC-free aerosols with hygroscopicity lower
418 than the critical κ value of 0.07; however, they were still CCN-active and therefore not fully
419 hydrophobic.

420 The diurnal variations in MAF, NF_H , NF_V , and NF_{noBC} , along with the MFs of the aerosol
421 chemical components during the three periods, are shown in Fig. 4. Except for a particle size of 50 nm,
422 the diurnal variations in these four mixing state parameters were generally similar for all measured
423 sizes. The different diurnal variations at a particle size of 50 nm may be due to the different effects of
424 emissions and aging processes on the different aerosol modes, as particles < 100 nm mainly reside in
425 the Aitken mode, which is where particles > 100 nm mainly reside in the accumulation mode (Wang et
426 al., 2022). For particles > 100 nm (Fig. 4 and S5), there was a maximum in the afternoon for MAF,
427 NF_H , NF_V , and NF_{noBC} , indicating a peak during this time due to an increase in SA compositions, such
428 as nitrate and SOA, and a decrease in POA and BC. Diurnal variations in the aerosol mixing state
429 parameters and chemical compositions were more pronounced during the moderately polluted period.

430 During heavily polluted periods, the diurnal variation was least pronounced for NF_V and most
431 pronounced for NF_H . In the clean-air period, there was another maximum at midnight for MAF and
432 NF_{noBC} , which may be attributed to the diurnal variations in SA compositions, such as sulfate and SOA,
433 and the decrease in BC and FFOA. The average-size dependence of the aerosol mixing state parameters
434 over different time ranges during a heavily polluted period is shown in Fig. S6. It can be seen that the
435 differences among the four parameters were the least from 12:00 to 18:00, with the most SOA and the
436 least POA. This is consistent with the results shown in Fig. 3, where the difference between the MAF
437 and NF_H decreased when the POA fractions were the smallest. R_{exBC} tended to be lower during the
438 daytime, and its diurnal variation was more significant for larger particle sizes. In general, the diurnal
439 variations for R_{exBC} were opposite to those of NF_{noBC} and agreed better with those of the primary
440 aerosol MFs. This is because BC particles originate from primary emissions and are mainly mixed
441 externally. After aging in the atmosphere, BC particles can be coated by SAs, resulting in more coated
442 BC particles and fewer externally mixed BC particles. As SAs tend to form on larger particles, the
443 diurnal variations in SA formation may significantly affect the R_{exBC} of larger particle sizes.

444 As summarized in Table. S1, the comparison among MAF, NF_H , NF_V , and NF_{noBC} was
445 conducted based on their correlations with different particle sizes. Note that the MAF at SSs of 0.08%,
446 0.14%, and 0.22% were used for comparison at 200, 150, and 100 nm particle sizes. This is because
447 the diameter range of rapid increases in the SPAR curves is determined by aerosol hygroscopicity in
448 this particle size range. The midpoints of the rapidly increasing diameter ranges of the SPAR curves
449 at SSs of 0.08%, 0.14%, and 0.22% were approximately 180 nm, 120 nm, and 90 nm, respectively (as
450 shown in Fig. 2). In general, there were moderate correlations ($r \sim 0.5$) between MAF, NF_H , and NF_V ,
451 suggesting that a similar particle group contributed to the dominance of CCN-active, hygroscopic, and
452 volatile aerosols (Zhang et al., 2016). The agreement between MAF and NF_V was slightly higher than
453 that between MAF and NF_H or between NF_H and NF_V with similar correlation coefficients (~ 0.65).
454 However, smaller systematic differences (slope and intercept) were much closer to 1 and 0,
455 respectively. This is consistent with the previous finding that a substantial fraction of volatile but less
456 hygroscopic aerosols are CCN-active. For smaller particle sizes, the correlation became weaker
457 ($r \sim 0.4$), whereas the degree of reduction was the lowest for the correlation between MAF and NF_V .

458 3.3 Impacts of primary aerosol emissions on aerosol mixing states and parameter 459 intercomparisons

460 Fig. 5 presents the correlation between each aerosol mixing state parameter at 200 nm and the
461 MF of each primary organic aerosol composition during the three periods. The four mixing state
462 parameters (MAF, N_{F_H} , N_{F_V} , and $N_{F_{noBC}}$) were negatively correlated with MF_{FFOA} and MF_{BBOA} .
463 However, the anticorrelation with MF_{FFOA} (-0.45~-0.74) was much stronger than MF_{BBOA} (-0.10~-
464 0.45). Biomass-burning emissions and fossil fuel emissions are the two major sources of BC in the
465 NCP (Yang et al., 2022), and $N_{F_{noBC}}$ was negatively correlated with MF_{FFOA} ($r=-0.49$) and weakly
466 correlated ($r=-0.18$) with MF_{BBOA} , suggesting that fossil fuel emissions were likely the dominant
467 source of BC during this field campaign. The negative correlation between MAF and MF_{FFOA} was
468 weaker than that of $N_{F_{noBC}}$ with MF_{FFOA} (-0.62 vs. -0.49). In particular, at the same MF_{FFOA} , the MAF
469 was lower than $N_{F_{noBC}}$, demonstrating that some BC-free particles were CCN-inactive and were likely
470 mainly composed of organic aerosols from fossil fuel combustion emissions. The negative correlation
471 between N_{F_V} and MF_{FFOA} was slightly weaker than between $N_{F_{noBC}}$ and MF_{FFOA} (-0.56 vs. -0.49). At
472 the same MF_{FFOA} , $N_{F_{noBC}}$ was close to N_{F_V} , and considering that BC-containing aerosols were
473 dominated by thinly coated BC most of the time (Fig. 5), this demonstrates that the non-volatile
474 population identified by V-TDMA was mainly contributed by BC-containing aerosols. N_{F_H} had the
475 lowest negative correlation with MF_{FFOA} ($r=-0.74$), demonstrating significant contributions from fossil
476 fuel emissions to nearly hydrophobic aerosol populations. At the same MF_{FFOA} , N_{F_H} was obviously
477 lower than $N_{F_{noBC}}$ (N_{F_H} and $N_{F_{noBC}}$ were larger and smaller than 0.7 when MF_{FFOA} was larger than
478 0.1), demonstrating that a substantial portion of nearly hydrophobic aerosols was not contributed by
479 BC-containing aerosols (BC-containing aerosols of 200 nm with BC core smaller than 80 nm which is
480 smaller than the detection limit of SP2 likely to be quite aged in the air, thus not possible to be nearly
481 hydrophobic), but likely by FFOA- or BBOA-dominant aerosols (N_{F_H} also had a negative correlation
482 with MF_{BBOA}). However, the markedly different correlations between MAF and MF_{FFOA} ($r=-0.62$) and
483 between MAF and MF_{BBOA} ($r=-0.2$) imply that nearly hydrophobic but CCN-active aerosols were
484 likely contributed by biomass-burning emissions. The correlations between the ratio of thinly coated
485 BC in the total BC-containing particles (R_{exBC}) and the MFs of BBOA and FFOA are shown in Fig. 6.
486 Weak correlations ($r<0.3$) between R_{exBC} and MF_{BBOA} and MF_{FFOA} were observed. However, R_{exBC}

487 tended to increase with MF_{FFOA} , suggesting that BC-containing aerosols emitted from fossil fuel
488 combustion tended to be more externally mixed with other aerosol components than those emitted
489 from biomass burning. These results demonstrate remarkably different mixing states and the physical
490 and chemical properties of fossil fuel combustion and biomass-burning aerosols.

491 The impact of primary emissions on the differences among the four aerosol mixing state
492 parameters at a particle size of 200 nm was analyzed and is shown in Fig. 7. The difference between
493 NF_{noBC} and NF_H ($NF_{noBC}-NF_H$) was significantly positively correlated with MF_{FFOA} and MF_{BBOA}
494 ($r>0.5$), suggesting that a substantial proportion of POA resided in BC-free aerosols and was volatile,
495 but contributed substantially to nearly hydrophobic aerosols; as did the differences between NF_V and
496 NF_H (NF_V-NF_H). The MFs of BBOA and FFOA were poorly correlated with the differences between
497 the MAF and NF_V ($MAF-NF_V$), MAF and NF_{noBC} ($MAF-NF_{noBC}$), and NF_V and NF_{noBC} (NF_V-NF_{noBC})
498 (Fig. S7). The difference between $MAF-NF_H$ was positively correlated with MF_{BBOA} , further
499 suggesting that BBOA contributed to nearly hydrophobic aerosols under subsaturated conditions;
500 however, their hygroscopicity was enhanced, and they became CCN-active under supersaturated
501 conditions. The correlations between the mixing-state parameters and primary aerosol composition
502 during the campaign and different pollution periods are summarized in Fig. S7.

503

504 **3.4 Impacts of SA formation on aerosol mixing states and parameter intercomparisons**

505 The correlations between the aerosol mixing state parameters at 200 nm and the MF of each SA
506 component are presented in Fig. 8 for three periods, and the entire campaign is presented. The analysis
507 is conducted at only 200 nm, where all four aerosol mixing state parameters were measured to compare
508 the four aerosol mixing state parameters and their relationships with aerosol chemical compositions
509 simultaneously. Generally, MAF, NF_H , NF_V , and NF_{noBC} exhibited strong positive correlations with
510 MF_{NH4} ($r>0.5$). This is likely because ammonium was mainly formed through neutralizing sulfuric and
511 nitric acids with ammonia; therefore, variations in ammonium better represent overall secondary
512 inorganic aerosol formation. As shown in Fig. 3, the secondary inorganic aerosol components
513 dominated over SA (approximately 50% vs. approximately 70%), indicating that SA formation was
514 primarily composed of secondary inorganic aerosol formation, which explains the weaker correlation
515 with SOA ($r\sim 0.3$), as shown in Fig. 8.

516 During the clean-air period, when the MFs of SOA and sulfate were both above 15%, all four
517 parameters had a strong positive correlation with MF_{SO_4} and MF_{SOA} ($r > 0.5$), suggesting that when a
518 clean background air mass with higher fractions of sulfate and SOA prevailed, the local primary
519 emissions that contributed substantially to BC-containing and less hygroscopic POA aerosols became
520 less significant. The positive correlations between the MAF and SA components have been extensively
521 discussed by Tao et al. (2021), who found that SA formation enhances the hygroscopicity of nearly
522 hydrophobic aerosols, thereby increasing CCN activity. This also explains the strong correlation
523 between the NF_H or MAF and ammonium formation. The strong positive correlations between NF_V
524 and SA formation ($r \sim 0.6$) are consistent with the fact that nitrate dominates SA formation during this
525 campaign and is semi-volatile. For the first time, strong positive correlations between NF_{noBC} and SA
526 formation were observed ($r = 0.6$). NF_{noBC} depends primarily on the relative variation between BC-
527 containing and BC-free aerosols. The increase in NF_{noBC} at 200 nm as a function of the SA MF suggests
528 that SAs migrated to a higher fraction of BC-free aerosols smaller than 200 nm to particle size of 200
529 nm, highlighting that SAs tended to form more quickly on BC-free aerosols than on BC-containing
530 aerosols.

531 The effects of SA formation on the differences between the four aerosol mixing state parameters
532 were studied and are illustrated in Fig. 9. The two OOA factors (OOA1 and OOA2) were formed
533 through different chemical pathways. The difference between NF_{noBC} and NF_H ($NF_{noBC} - NF_H$) showed
534 a strong negative correlation with MF_{NH_4} and MF_{NO_3} (mainly -0.6), as did the differences between NF_V
535 and NF_H ($NF_V - NF_H$). As previously noted, NF_H typically has smaller values than NF_V and NF_{noBC} .
536 Thus, a negative correlation between the MFs of ammonium and nitrate indicated that the formation
537 of secondary nitrate resulted in a smaller difference between these mixing state parameters. An
538 increase in the fraction of ammonium nitrate, a pure-scattering semi-volatile compound with strong
539 hygroscopicity, can render the aerosol population more dominated by particles with strong volatility
540 and hygroscopicity. As the secondary inorganic aerosol components increase, this can result in a
541 smaller difference between NF_{noBC} , NF_H , and NF_V .

542 Furthermore, the difference between NF_V and NF_H showed a positive correlation with MF_{OOA2}
543 and a negative correlation with MF_{OOA1} , indicating different volatility and hygroscopicity of the two
544 SOA factors. The differences between NF_V and NF_H concerning the MF of OOA1 and OOA2 are

545 shown in Fig. 9(e) and (f), respectively. As previously noted, NF_V was generally higher than NF_H , and
546 the difference between the two decreased with increasing MF_{OOA1} , which was generally smaller than
547 0.3. This suggests that the formation of OOA1 enhances the hygroscopicity of volatile particles, which
548 aligns with the highest oxidation state of OOA1 (higher O/C but lower H/C compared to OOA2) and
549 has a significant and overall positive impact on aerosol hygroscopicity (Cerully et al., 2015; Thalman
550 et al., 2017; Zhang et al., 2023). A positive correlation was observed between NF_V and MF_{OOA2}
551 ($r \sim -0.25$).

552 In contrast, the correlation between NF_H and MF_{OOA2} was weak (R was close to 0), implying that
553 OOA2 might be semi-volatile but only weakly hygroscopic, which could contribute to NF_V being
554 higher than NF_H as OOA1 increases. The difference between NF_{noBC} and NF_V ($NF_{noBC} - NF_V$) was
555 negatively correlated with MF_{NO3} , which is consistent with the semi-volatile nature of nitrate. The
556 negative correlation between $NF_{noBC} - NF_V$ and MF_{OOA2} indicates that the difference is smaller when
557 there is more OOA2, implying that OOA2 is also a semi-volatile compound and is likely formed
558 mainly on BC-free particles. The correlations between the differences between $NF_V - MAF$ and $NF_{noBC} -$
559 MAF and the MF of each SA composition were very weak. The impacts of SA formation on BC mixing
560 states are shown in Fig. S8. In general, the NF of thinly coated BC has a negative correlation with SIA
561 and a weak association with SOA, suggesting that SIA formation mainly enhances the thickness of the
562 BC coating. The correlations between the mixing state parameters and SA composition during the
563 campaign and different pollution periods are summarized in Fig. S9.

564 In addition to changes in the MFs of SA compositions, the accumulation of SA pollution may
565 provide insights into the impact of SA formation on aerosol mixing states. As shown in Fig. 10(a),
566 during the heavily polluted periods, there were two distinct pollution accumulation processes from the
567 23rd to the 27th of October and from the 28th to the 31st of October, respectively. During the pollution
568 accumulation process, the mass concentration of SAs increased by approximately three-fold, indicating
569 the rapid formation of secondary compositions and a significant increase in non-refractory PM_1 (NR-
570 PM_1) mass concentration. Fig. 10(b) and (c) illustrate that this increase in SAs significantly enhanced
571 aerosol mixing state parameters, including MAF, NF_V , NF_H , and NF_{noBC} , which increased from
572 approximately 0.5 to 0.8 with evident diurnal variations. This highlights the impact of SA formation
573 on the aerosol mixing states and the importance of studying the pollution accumulation processes of

574 SAs. The enhancements in the different aerosol mixing state parameters during the pollution
575 accumulation process were not uniform. MAF and NF_H initially exhibited lower values than NF_V and
576 NF_{noBC} ; however, their later enhancement was stronger than that of NF_{noBC} . Fig. 10(d) and (e) show
577 the difference between NF_{noBC} and NF_V at 200 and 300 nm as a function of SA mass concentrations
578 during these two pollution periods, which clearly shows how, during SA formation, NF_V became
579 higher than NF_{noBC} while NF_V remained close to the NF of thickly coated BC-containing aerosols
580 (NF_{CBC}) plus NF_{noBC} ($NF_{CBC}+NF_{CBC}$). These results suggest that SA formation increases the volatility
581 of BC-free and BC-containing aerosols, leading to an increased NF_V compared with NF_{noBC} . Almost
582 all BC-free particles and some BC-containing aerosols become volatile during the accumulation of
583 pollution.

584

585 **4. Conclusions**

586 The aerosol mixing state is one of the most important physicochemical properties of aerosol
587 particles and significantly affects their optical properties and the CCN activity of aerosol particles. The
588 aerosol mixing states vary significantly with complex aerosol emissions and atmospheric
589 transformations. In this study, aerosol mixing states derived from CCN activity, hygroscopicity,
590 volatility, and BC particle observations, along with their relationship to primary aerosol emissions and
591 SA formation, were systematically analyzed based on simultaneous measurements of CCNC,
592 H/VTDMA, and SP2. Statistical analysis demonstrated that the NFs of CCN-active, hygroscopic, and
593 volatile particles were generally positively correlated and mainly contributed by BC-free aerosols.
594 Therefore, four mixing state parameters were all negatively correlated to either the MFs of BBOA or
595 FFOA because fossil fuel combustion and biomass burning were the two major sources of BC-
596 containing aerosols during this field campaign. However, the differences between these mixing state
597 parameters vary significantly under different conditions.

598 The intercomparison results highlight the differences in the aerosol mixing states and
599 physicochemical properties caused by fossil fuel combustion and biomass-burning emissions. The
600 CCN and SP2 measurements showed that CCN-inactive BC-free particles were mainly produced by
601 fossil fuel combustion. In contrast, a comparison between the VTDMA and SP2 measurements
602 indicated that the non-volatile aerosols mostly comprised BC-containing particles. The comparison

603 between HTDMA and SP2 measurements revealed that a significant proportion of nearly hydrophobic
604 aerosols was not from BC-containing particles but from fossil fuel combustion or biomass-burning-
605 dominated organic aerosols. The correlation between the CCNC and HTDMA measurements also
606 showed that nearly hydrophobic, BC-free aerosols could become CCN-active under supersaturated
607 conditions and are tightly linked to biomass-burning emissions. This suggests that biomass-burning
608 aerosols may exhibit different hygroscopicities under sub- and supersaturated conditions (Bougiatioti
609 et al., 2016). Furthermore, the correlation analysis between SP2 measurements and the MFs of BBOA
610 and FFOA indicated that BC-containing aerosols from fossil fuel combustion tended to be more
611 externally mixed with other aerosol compositions than those from biomass burning activities.

612 In addition to primary aerosol emissions, SA formation also significantly impacts variations in
613 aerosol mixing states. During this campaign, SA formation was dominated by nitrate and SOA
614 production, which had markedly different impacts on the aerosol mixing states owing to their different
615 physical properties and formation pathways. NF_{noBC} , MAF, NF_H , and NF_V were all positively
616 correlated with the nitrate and SOA MFs, revealing much stronger correlations with SOA than nitrate.
617 This is consistent with the semi-volatile but highly hygroscopic properties of nitrates. The high
618 correlation coefficient between NF_{noBC} and the MFs of SAs at 200 and 300 nm suggests that SA
619 formation led to the migration of BC-free aerosols towards larger diameters more quickly than that of
620 BC-containing aerosols. This result reveals that SAs formed more rapidly on BC-free than on BC-
621 containing aerosols, which aligns with the hydrophobic nature of BC-containing aerosols that do not
622 favor aqueous SA formation. Moreover, as the MFs of nitrate or ammonium increased, the differences
623 between the mixing-state parameters (NF_{noBC} , MAF, NF_H , and NF_V) decreased because of the
624 hygroscopic and semi-volatile nature of ammonium nitrate. However, the two resolved SOA factors
625 exhibited different impacts on the differences between NF_V and NF_H ($NF_V - NF_H$), and their correlations
626 with NF_V and NF_H revealed that OOA1 was more hygroscopic but less volatile, suggesting distinct
627 formation mechanisms for these two OOA factors during the field campaign.

628 The findings of this study highlight the markedly different effects of primary emissions and SA
629 formation on aerosol mixing states and suggest that comparisons of aerosol mixing states obtained
630 using various techniques are useful for gaining insights into the hygroscopicity, volatility, and CCN
631 activity of different aerosols. These comparisons also indicate the impact of SA formation on aerosol

632 physical properties, which can help understand the pathways of SA formation. However, it is important
633 to be cautious in the application of aerosol mixing state parameters because the suitability of VTDMA-
634 derived mixing state parameters for representing BC mixing states is largely dependent on the
635 composition and mass of the SAs.

636

637 **Data availability.** The data used in this study are available from the corresponding author upon request
638 Ye Kuang (kuangye@jnu.edu.cn) and Li Liu (liul@gd121.cn)

639 **Competing interests.** The authors declare that they have no conflict of interest.

640

641 **Author Contributions.**

642 YK and WY planned this campaign and YK designed the aerosol experiments and conceived this
643 research together with JC, and JC wrote the manuscript. JC performed measurements of CCNC, BL
644 performed measurements of SP2 and analyzed SP2 datasets with the help of GZ, WQ and YL
645 performed AMS measurements, LL performed HV-TDMA measurements and conducted post-data
646 processing as well as some of data analysis. BX, HX, MMZ, HZ and SR participated this campaign
647 and helped instruments maintenance. GZ provided full support for the campaign. All authors
648 contributed to discussions and revisions of this paper.

649 **Financial supports.** This work is supported by National Natural Science Foundation of China
650 (42175083, 42175127, 42275066), the Guangzhou Science and Information Technology Bureau
651 Project (2023A04J0941), the Guangdong Provincial Key Research and Development Program (grant
652 no. 2020B1111360003), the Science and Technology Innovation Team Plan of Guangdong
653 Meteorological Bureau (grant no. GRMCTD202003).

654

655 **References**

656 Adachi, K., Sedlacek, A. J., Kleinman, L., Chand, D., Hubbe, J. M., and Buseck, P. R.: Volume
657 changes upon heating of aerosol particles from biomass burning using transmission electron
658 microscopy, *Aerosol Science and Technology*, 52, 46–56,
659 <https://doi.org/10.1080/02786826.2017.1373181>, 2018.

660 Adachi, K., Sedlacek, A. J., Kleinman, L., Springston, S. R., Wang, J., Chand, D., Hubbe, J. M.,
661 Shilling, J. E., Onasch, T. B., Kinase, T., Sakata, K., Takahashi, Y., and Buseck, P. R.: Spherical tarball
662 particles form through rapid chemical and physical changes of organic matter in biomass-burning
663 smoke, *Proceedings of the National Academy of Sciences*, 116, 19336–19341,
664 <https://doi.org/10.1073/pnas.1900129116>, 2019.

665 Bond, T. C., Doherty, S. J., Fahey, D. W., Forster, P. M., Berntsen, T., DeAngelo, B. J., Flanner,
666 M. G., Ghan, S., Kaercher, B., Koch, D., Kinne, S., Kondo, Y., Quinn, P. K., Sarofim, M. C., Schultz,
667 M. G., Schulz, M., Venkataraman, C., Zhang, H., Zhang, S., Bellouin, N., Guttikunda, S. K., Hopke,
668 P. K., Jacobson, M. Z., Kaiser, J. W., Klimont, Z., Lohmann, U., Schwarz, J. P., Shindell, D.,
669 Storelvmo, T., Warren, S. G., and Zender, C. S.: Bounding the role of black carbon in the climate
670 system: A scientific assessment, *Journal of Geophysical Research-Atmospheres*, 118, 5380–5552,
671 <https://doi.org/10.1002/jgrd.50171>, 2013.

672 Bougiatioti, A., Bezantakos, S., Stavroulas, I., Kalivitis, N., Kokkalis, P., Biskos, G.,
673 Mihalopoulos, N., Papayannis, A., and Nenes, A.: Biomass-burning impact on CCN number,
674 hygroscopicity and cloud formation during summertime in the eastern Mediterranean, *Atmos. Chem.*
675 *Phys.*, 16, 7389–7409, <https://doi.org/10.5194/acp-16-7389-2016>, 2016.

676 Cai, M., Tan, H., Chan, C. K., Mochida, M., Hatakeyama, S., Kondo, Y., Schurman, M. I., Xu,
677 H., Li, F., Shimada, K., Li, L., Deng, Y., Yai, H., Matsuki, A., Qin, Y., and Zhao, J.: Comparison of
678 Aerosol Hygroscopicity, Volatility, and Chemical Composition between a Suburban Site in the Pearl
679 River Delta Region and a Marine Site in Okinawa, *Aerosol and Air Quality Research*, 17, 3194–3208,
680 <https://doi.org/10.4209/aaqr.2017.01.0020>, 2017.

681 Canagaratna, M. R., Jimenez, J. L., Kroll, J. H., Chen, Q., Kessler, S. H., Massoli, P., Hildebrandt
682 Ruiz, L., Fortner, E., Williams, L. R., Wilson, K. R., Surratt, J. D., Donahue, N. M., Jayne, J. T., and
683 Worsnop, D. R.: Elemental ratio measurements of organic compounds using aerosol mass
684 spectrometry: characterization, improved calibration, and implications, *Atmos. Chem. Phys.*, 15, 253–
685 272, <https://doi.org/10.5194/acp-15-253-2015>, 2015.

686 Cerully, K. M., Bougiatioti, A., Hite Jr., J. R., Guo, H., Xu, L., Ng, N. L., Weber, R., and Nenes,
687 A.: On the link between hygroscopicity, volatility, and oxidation state of ambient and water-soluble
688 aerosols in the southeastern United States, *Atmos. Chem. Phys.*, 15, 8679–8694,
689 <https://doi.org/10.5194/acp-15-8679-2015>, 2015.

690 Chen, C., Qiu, Y., Xu, W., He, Y., Li, Z., Sun, J., Ma, N., Xu, W., Pan, X., Fu, P., Wang, Z., and
691 Sun, Y.: Primary Emissions and Secondary Aerosol Processing During Wintertime in Rural Area of
692 North China Plain, *Journal of Geophysical Research: Atmospheres*, 127, e2021JD035430,
693 <https://doi.org/10.1029/2021JD035430>, 2022.

694 Chen, J., Budisulistiorini, S. H., Miyakawa, T., Komazaki, Y., and Kuwata, M.: Secondary
695 aerosol formation promotes water uptake by organic-rich wildfire haze particles in equatorial Asia,
696 *Atmos. Chem. Phys.*, 18, 7781–7798, <https://doi.org/10.5194/acp-18-7781-2018>, 2018.

697 Cheng, Y. F., Su, H., Rose, D., Gunthe, S. S., Berghof, M., Wehner, B., Achtert, P., Nowak, A.,
698 Takegawa, N., Kondo, Y., Shiraiwa, M., Gong, Y. G., Shao, M., Hu, M., Zhu, T., Zhang, Y. H.,
699 Carmichael, G. R., Wiedensohler, A., Andreae, M. O., and Pöschl, U.: Size-resolved measurement of
700 the mixing state of soot in the megacity Beijing, China: diurnal cycle, aging and parameterization,
701 *Atmos. Chem. Phys.*, 12, 4477–4491, <https://doi.org/10.5194/acp-12-4477-2012>, 2012.

702 Ching, J., Fast, J., West, M., and Riemer, N.: Metrics to quantify the importance of mixing state
703 for CCN activity, *Atmos. Chem. Phys.*, 17, 7445–7458, <https://doi.org/10.5194/acp-17-7445-2017>,
704 2017.

705 Ching, J., Adachi, K., Zaizen, Y., Igarashi, Y., and Kajino, M.: Aerosol mixing state revealed by
706 transmission electron microscopy pertaining to cloud formation and human airway deposition, *npj*
707 *Climate and Atmospheric Science*, 2, 22, <https://doi.org/10.1038/s41612-019-0081-9>, 2019.

708 Deng, Z. Z., Zhao, C. S., Ma, N., Liu, P. F., Ran, L., Xu, W. Y., Chen, J., Liang, Z., Liang, S.,
709 Huang, M. Y., Ma, X. C., Zhang, Q., Quan, J. N., Yan, P., Henning, S., Mildenberger, K., Sommerhage,
710 E., Schäfer, M., Stratmann, F., and Wiedensohler, A.: Size-resolved and bulk activation properties of
711 aerosols in the North China Plain, *Atmos. Chem. Phys.*, 11, 3835–3846, [https://doi.org/10.5194/acp-](https://doi.org/10.5194/acp-11-3835-2011)
712 11-3835-2011, 2011.

713 Deng, Z. Z., Zhao, C. S., Ma, N., Ran, L., Zhou, G. Q., Lu, D. R., and Zhou, X. J.: An examination
714 of parameterizations for the CCN number concentration based on in situ measurements of aerosol
715 activation properties in the North China Plain, *Atmos. Chem. Phys.*, 13, 6227–6237,
716 <https://doi.org/10.5194/acp-13-6227-2013>, 2013.

717 Drinovec, L., Močnik, G., Zotter, P., Prévôt, A. S. H., Ruckstuhl, C., Coz, E., Rupakheti, M.,
718 Sciare, J., Müller, T., Wiedensohler, A., and Hansen, A. D. A.: The “dual-spot” Aethalometer: an
719 improved measurement of aerosol black carbon with real-time loading compensation, *Atmos. Meas.*
720 *Tech.*, 8, 1965–1979, <https://doi.org/10.5194/amt-8-1965-2015>, 2015.

721 Ervens, B.: Modeling the Processing of Aerosol and Trace Gases in Clouds and Fogs, *Chemical*
722 *Reviews*, 115, 4157–4198, <https://doi.org/10.1021/cr5005887>, 2015.

723 Farmer, D. K., Cappa, C. D., and Kreidenweis, S. M.: Atmospheric Processes and Their
724 Controlling Influence on Cloud Condensation Nuclei Activity, *Chemical Reviews*, 115, 4199–4217,
725 <https://doi.org/10.1021/cr5006292>, 2015.

726 Fierce, L., Riemer, N., and Bond, T. C.: Toward Reduced Representation of Mixing State for
727 Simulating Aerosol Effects on Climate, *Bulletin of the American Meteorological Society*, 98, 971–
728 980, <https://doi.org/10.1175/BAMS-D-16-0028.1>, 2017.

729 Fu, Y., Peng, X., Sun, W., Hu, X., Wang, D., Yang, Y., Guo, Z., Wang, Y., Zhang, G., Zhu, J.,
730 Ou, J., Shi, Z., Wang, X., and Bi, X.: Impact of Cloud Process in the Mixing State and Microphysical
731 Properties of Soot Particles: Implications in Light Absorption Enhancement, *Journal of Geophysical*
732 *Research: Atmospheres*, n/a, e2022JD037169, <https://doi.org/10.1029/2022JD037169>, 2022.

733 Gysel, M., Laborde, M., Olfert, J. S., Subramanian, R., and Gröhn, A. J.: Effective density of
734 Aquadag and fullerene soot black carbon reference materials used for SP2 calibration, *Atmos. Meas.*
735 *Tech.*, 4, 2851–2858, <https://doi.org/10.5194/amt-4-2851-2011>, 2011.

736 Herich, H., Kammermann, L., Gysel, M., Weingartner, E., Baltensperger, U., Lohmann, U., and
737 Cziczo, D. J.: In situ determination of atmospheric aerosol composition as a function of hygroscopic
738 growth, *Journal of Geophysical Research: Atmospheres*, 113, <https://doi.org/10.1029/2008JD009954>,
739 2008.

740 Herich, H., Kammermann, L., Friedman, B., Gross, D. S., Weingartner, E., Lohmann, U.,
741 Spichtinger, P., Gysel, M., Baltensperger, U., and Cziczo, D. J.: Subarctic atmospheric aerosol
742 composition: 2. Hygroscopic growth properties, *Journal of Geophysical Research: Atmospheres*, 114,
743 <https://doi.org/10.1029/2008JD011574>, 2009.

744 Hong, J., Äijälä, M., Häme, S. A. K., Hao, L., Duplissy, J., Heikkinen, L. M., Nie, W., Mikkilä,
745 J., Kulmala, M., Prisle, N. L., Virtanen, A., Ehn, M., Paasonen, P., Worsnop, D. R., Riipinen, I., Petäjä,
746 T., and Kerminen, V.-M.: Estimates of the organic aerosol volatility in a boreal forest using two
747 independent methods, *Atmos. Chem. Phys.*, 17, 4387–4399, [https://doi.org/10.5194/acp-17-4387-](https://doi.org/10.5194/acp-17-4387-2017)
748 2017, 2017.

749 Jayne, J. T., Leard, D. C., Zhang, X., Davidovits, P., Smith, K. A., Kolb, C. E., and Worsnop, D.
750 R.: Development of an Aerosol Mass Spectrometer for Size and Composition Analysis of Submicron
751 Particles, *Aerosol Science and Technology*, 33, 49–70, <https://doi.org/10.1080/027868200410840>,
752 2000.

753 Jiang, X., Tao, J., Kuang, Y., Hong, J., and Ma, N.: Mathematical derivation and physical
754 interpretation of particle size-resolved activation ratio based on particle hygroscopicity distribution:
755 Application on global characterization of CCN activity, *Atmospheric Environment*, 246, 118137,
756 <https://doi.org/10.1016/j.atmosenv.2020.118137>, 2021.

757 Jurányi, Z., Tritscher, T., Gysel, M., Laborde, M., Gomes, L., Roberts, G., Baltensperger, U., and
758 Weingartner, E.: Hygroscopic mixing state of urban aerosol derived from size-resolved cloud
759 condensation nuclei measurements during the MEGAPOLI campaign in Paris, *Atmos. Chem. Phys.*,
760 13, 6431–6446, <https://doi.org/10.5194/acp-13-6431-2013>, 2013.

761 Kawana, K., Nakayama, T., and Mochida, M.: Hygroscopicity and CCN activity of atmospheric
762 aerosol particles and their relation to organics: Characteristics of urban aerosols in Nagoya, Japan,
763 *Journal of Geophysical Research: Atmospheres*, 121, 4100–4121,
764 <https://doi.org/10.1002/2015jd023213>, 2016.

765 Kim, N., Yum, S. S., Park, M., Park, J. S., Shin, H. J., and Ahn, J. Y.: Hygroscopicity of urban
766 aerosols and its link to size-resolved chemical composition during spring and summer in Seoul, Korea,
767 *Atmos. Chem. Phys.*, 20, 11245–11262, <https://doi.org/10.5194/acp-20-11245-2020>, 2020.

768 Kuang, Y., Zhao, C. S., Tao, J. C., and Ma, N.: Diurnal variations of aerosol optical properties in
769 the North China Plain and their influences on the estimates of direct aerosol radiative effect, *Atmos.*
770 *Chem. Phys.*, 15, 5761–5772, <https://doi.org/10.5194/acp-15-5761-2015>, 2015.

771 Kuang, Y., He, Y., Xu, W., Yuan, B., Zhang, G., Ma, Z., Wu, C., Wang, C., Wang, S., Zhang, S.,
772 Tao, J., Ma, N., Su, H., Cheng, Y., Shao, M., and Sun, Y.: Photochemical Aqueous-Phase Reactions

773 Induce Rapid Daytime Formation of Oxygenated Organic Aerosol on the North China Plain,
774 *Environmental Science & Technology*, 54, 3849–3860, <https://doi.org/10.1021/acs.est.9b06836>, 2020.

775 Kuang, Y., Huang, S., Xue, B., Luo, B., Song, Q., Chen, W., Hu, W., Li, W., Zhao, P., Cai, M.,
776 Peng, Y., Qi, J., Li, T., Wang, S., Chen, D., Yue, D., Yuan, B., and Shao, M.: Contrasting effects of
777 secondary organic aerosol formations on organic aerosol hygroscopicity, *Atmos. Chem. Phys.*, 21,
778 10375–10391, <https://doi.org/10.5194/acp-21-10375-2021>, 2021.

779 Kuwata, M. and Kondo, Y.: Dependence of size-resolved CCN spectra on the mixing state of
780 nonvolatile cores observed in Tokyo, *Journal of Geophysical Research: Atmospheres*, 113,
781 <https://doi.org/10.1029/2007JD009761>, 2008.

782 Kuwata, M., Kondo, Y., Mochida, M., Takegawa, N., and Kawamura, K.: Dependence of CCN
783 activity of less volatile particles on the amount of coating observed in Tokyo, *Journal of Geophysical*
784 *Research: Atmospheres*, 112, <https://doi.org/10.1029/2006JD007758>, 2007.

785 Lack, D. A., Langridge, J. M., Bahreini, R., Cappa, C. D., Middlebrook, A. M., and Schwarz, J.
786 P.: Brown carbon and internal mixing in biomass burning particles, *Proceedings of the National*
787 *Academy of Sciences*, 109, 14802–14807, <https://doi.org/10.1073/pnas.1206575109>, 2012.

788 Lance, S., Nenes, A., Medina, J., and Smith, J. N.: Mapping the operation of the DMT continuous
789 flow CCN counter, *Aerosol science and technology*, 40, 242–254, 2006.

790 Lance, S., Raatikainen, T., Onasch, T. B., Worsnop, D. R., Yu, X. Y., Alexander, M. L.,
791 Stolzenburg, M. R., McMurry, P. H., Smith, J. N., and Nenes, A.: Aerosol mixing state, hygroscopic
792 growth and cloud activation efficiency during MIRAGE 2006, *Atmos. Chem. Phys.*, 13, 5049–5062,
793 <https://doi.org/10.5194/acp-13-5049-2013>, 2013.

794 Lata, N. N., Zhang, B., Schum, S., Mazzoleni, L., Brimberry, R., Marcus, M. A., Cantrell, W. H.,
795 Fialho, P., Mazzoleni, C., and China, S.: Aerosol Composition, Mixing State, and Phase State of Free
796 Tropospheric Particles and Their Role in Ice Cloud Formation, *ACS Earth Space Chem.*, 5, 3499–
797 3510, <https://doi.org/10.1021/acsearthspacechem.1c00315>, 2021.

798 Lee, A. K. Y., Rivellini, L.-H., Chen, C.-L., Liu, J., Price, D. J., Betha, R., Russell, L. M., Zhang,
799 X., and Cappa, C. D.: Influences of Primary Emission and Secondary Coating Formation on the
800 Particle Diversity and Mixing State of Black Carbon Particles, *Environ. Sci. Technol.*, 53, 9429–9438,
801 <https://doi.org/10.1021/acs.est.9b03064>, 2019.

802 Li, G., Su, H., Ma, N., Tao, J., Kuang, Y., Wang, Q., Hong, J., Zhang, Y., Kuhn, U., and Zhang,
803 S.: Multiphase chemistry experiment in Fogs and Aerosols in the North China Plain (McFAN):
804 integrated analysis and intensive winter campaign 2018, *Faraday Discussions*, 2021.

805 Liu, D., Joshi, R., Wang, J., Yu, C., Allan, J. D., Coe, H., Flynn, M. J., Xie, C., Lee, J., Squires,
806 F., Kotthaus, S., Grimmond, S., Ge, X., Sun, Y., and Fu, P.: Contrasting physical properties of black
807 carbon in urban Beijing between winter and summer, *Atmos. Chem. Phys.*, 19, 6749–6769,
808 <https://doi.org/10.5194/acp-19-6749-2019>, 2019.

809 Liu, D., Li, S., Hu, D., Kong, S., Cheng, Y., Wu, Y., Ding, S., Hu, K., Zheng, S., Yan, Q., Zheng,
810 H., Zhao, D., Tian, P., Ye, J., Huang, M., and Ding, D.: Evolution of Aerosol Optical Properties from
811 Wood Smoke in Real Atmosphere Influenced by Burning Phase and Solar Radiation, *Environ. Sci.*
812 *Technol.*, 55, 5677–5688, <https://doi.org/10.1021/acs.est.0c07569>, 2021.

813 Liu, K., Zhang, C., Cheng, Y., Liu, C., Zhang, H., Zhang, G., Sun, X., and Mu, Y.: Serious BTEX
814 pollution in rural area of the North China Plain during winter season, *Journal of Environmental*
815 *Sciences*, 30, 186–190, <https://doi.org/10.1016/j.jes.2014.05.056>, 2015.

816 Liu, P. F., Zhao, C. S., Göbel, T., Hallbauer, E., Nowak, A., Ran, L., Xu, W. Y., Deng, Z. Z., Ma,
817 N., and Mildenberger, K.: Hygroscopic properties of aerosol particles at high relative humidity and
818 their diurnal variations in the North China Plain, *Atmos. Chem. Phys.*, 11, 3479–3494, 2011.

819 Luo, B., Kuang, Y., Huang, S., Song, Q., Hu, W., Li, W., Peng, Y., Chen, D., Yue, D., Yuan, B.,
820 and Shao, M.: Parameterizations of size distribution and refractive index of biomass burning organic
821 aerosol with black carbon content, *Atmos. Chem. Phys.*, 22, 12401–12415,
822 <https://doi.org/10.5194/acp-22-12401-2022>, 2022.

823 Ma, N., Zhao, C. S., Müller, T., Cheng, Y. F., Liu, P. F., Deng, Z. Z., Xu, W. Y., Ran, L., Nekat,
824 B., van Pinxteren, D., Gnauk, T., Müller, K., Herrmann, H., Yan, P., Zhou, X. J., and Wiedensohler,
825 A.: A new method to determine the mixing state of light absorbing carbonaceous using the measured
826 aerosol optical properties and number size distributions, *Atmos. Chem. Phys.*, 12, 2381–2397,
827 <https://doi.org/10.5194/acp-12-2381-2012>, 2012.

828 Ma, N., Zhao, C., Tao, J., Wu, Z., Kecorius, S., Wang, Z., Größ, J., Liu, H., Bian, Y., Kuang, Y.,
829 Teich, M., Spindler, G., Müller, K., van Pinxteren, D., Herrmann, H., Hu, M., and Wiedensohler, A.:
830 Variation of CCN activity during new particle formation events in the North China Plain, *Atmos. Chem.*
831 *Phys.*, 16, 8593–8607, <https://doi.org/10.5194/acp-16-8593-2016>, 2016.

832 Matsui, H., Hamilton, D. S., and Mahowald, N. M.: Black carbon radiative effects highly sensitive
833 to emitted particle size when resolving mixing-state diversity, *Nature Communications*, 9, 3446,
834 <https://doi.org/10.1038/s41467-018-05635-1>, 2018.

835 Mei, F., Hayes, P. L., Ortega, A., Taylor, J. W., Allan, J. D., Gilman, J., Kuster, W., de Gouw, J.,
836 Jimenez, J. L., and Wang, J.: Droplet activation properties of organic aerosols observed at an urban
837 site during CalNex-LA, *Journal of Geophysical Research-Atmospheres*, 118, 2903–2917,
838 <https://doi.org/10.1002/jgrd.50285>, 2013.

839 Metcalf, A. R., Craven, J. S., Ensberg, J. J., Brioude, J., Angevine, W., Sorooshian, A., Duong,
840 H. T., Jonsson, H. H., Flagan, R. C., and Seinfeld, J. H.: Black carbon aerosol over the Los Angeles
841 Basin during CalNex, *Journal of Geophysical Research: Atmospheres*, 117,
842 <https://doi.org/10.1029/2011JD017255>, 2012.

843 Middlebrook, A. M., Bahreini, R., Jimenez, J. L., and Canagaratna, M. R.: Evaluation of
844 Composition-Dependent Collection Efficiencies for the Aerodyne Aerosol Mass Spectrometer using
845 Field Data, *Aerosol Science and Technology*, 46, 258–271,
846 <https://doi.org/10.1080/02786826.2011.620041>, 2012.

847 Moffet, R. C., O'Brien, R. E., Alpert, P. A., Kelly, S. T., Pham, D. Q., Gilles, M. K., Knopf, D.
848 A., and Laskin, A.: Morphology and mixing of black carbon particles collected in central California
849 during the CARES field study, *Atmos. Chem. Phys.*, 16, 14515–14525, [https://doi.org/10.5194/acp-](https://doi.org/10.5194/acp-16-14515-2016)
850 [16-14515-2016](https://doi.org/10.5194/acp-16-14515-2016), 2016.

851 Mohr, C., Huffman, J. A., Cubison, M. J., Aiken, A. C., Docherty, K. S., Kimmel, J. R., Ulbrich,
852 I. M., Hannigan, M., and Jimenez, J. L.: Characterization of Primary Organic Aerosol Emissions from

853 Meat Cooking, Trash Burning, and Motor Vehicles with High-Resolution Aerosol Mass Spectrometry
854 and Comparison with Ambient and Chamber Observations, *Environ. Sci. Technol.*, 43, 2443–2449,
855 <https://doi.org/10.1021/es8011518>, 2009.

856 Moteki, N. and Kondo, Y.: Effects of Mixing State on Black Carbon Measurements by Laser-
857 Induced Incandescence, *Aerosol Science and Technology*, 41, 398–417,
858 <https://doi.org/10.1080/02786820701199728>, 2007.

859 Nordmann, S., Cheng, Y. F., Carmichael, G. R., Yu, M., Denier van der Gon, H. A. C., Zhang,
860 Q., Saide, P. E., Pöschl, U., Su, H., Birmili, W., and Wiedensohler, A.: Atmospheric black carbon and
861 warming effects influenced by the source and absorption enhancement in central Europe, *Atmos. Chem.*
862 *Phys.*, 14, 12683–12699, <https://doi.org/10.5194/acp-14-12683-2014>, 2014.

863 Paatero, P. and Tapper, U.: Positive matrix factorization: A non-negative factor model with
864 optimal utilization of error estimates of data values, *Environmetrics*, 5, 111–126,
865 <https://doi.org/10.1002/env.3170050203>, 1994.

866 Peng, J., Hu, M., Guo, S., Du, Z., Zheng, J., Shang, D., Levy Zamora, M., Zeng, L., Shao, M.,
867 Wu, Y.-S., Zheng, J., Wang, Y., Glen, C. R., Collins, D. R., Molina, M. J., and Zhang, R.: Markedly
868 enhanced absorption and direct radiative forcing of black carbon under polluted urban environments,
869 *Proceedings of the National Academy of Sciences*, 113, 4266–4271,
870 <https://doi.org/10.1073/pnas.1602310113>, 2016.

871 Philippin, S., Wiedensohler, A., and Stratmann, F.: Measurements of non-volatile fractions of
872 pollution aerosols with an eight-tube volatility tandem differential mobility analyzer (VTDMA-8),
873 *Journal of Aerosol Science*, 35, 185–203, <https://doi.org/10.1016/j.jaerosci.2003.07.004>, 2004.

874 Ren, J., Zhang, F., Wang, Y., Collins, D., Fan, X., Jin, X., Xu, W., Sun, Y., Cribb, M., and Li, Z.:
875 Using different assumptions of aerosol mixing state and chemical composition to predict CCN
876 concentrations based on field measurements in urban Beijing, *Atmospheric Chemistry and Physics*,
877 18, 6907–6921, <https://doi.org/10.5194/acp-18-6907-2018>, 2018.

878 Riemer, N., Ault, A. P., West, M., Craig, R. L., and Curtis, J. H.: Aerosol Mixing State:
879 Measurements, Modeling, and Impacts, *Reviews of Geophysics*, 57, 187–249,
880 <https://doi.org/10.1029/2018RG000615>, 2019.

881 Roberts, G. C. and Nenes, A.: A continuous-flow streamwise thermal-gradient CCN chamber for
882 atmospheric measurements, *Aerosol science and technology*, 39, 206–221, 2005.

883 Rose, D., Gunthe, S. S., Mikhailov, E., Frank, G. P., Dusek, U., Andreae, M. O., and Pöschl, U.:
884 Calibration and measurement uncertainties of a continuous-flow cloud condensation nuclei counter
885 (DMT-CCNC): CCN activation of ammonium sulfate and sodium chloride aerosol particles in theory
886 and experiment, *Atmos. Chem. Phys.*, 8, 1153–1179, 2008.

887 Rose, D., Nowak, A., Achtert, P., Wiedensohler, A., Hu, M., Shao, M., Zhang, Y., Andreae, M.
888 O., and Pöschl, U.: Cloud condensation nuclei in polluted air and biomass burning smoke near the
889 mega-city Guangzhou, China - Part 1: Size-resolved measurements and implications for the modeling
890 of aerosol particle hygroscopicity and CCN activity, *Atmos. Chem. Phys.*, 10, 3365–3383, 2010.

891 Rose, D., Gunthe, S. S., Su, H., Garland, R. M., Yang, H., Berghof, M., Cheng, Y. F., Wehner,
892 B., Achtert, P., Nowak, A., Wiedensohler, A., Takegawa, N., Kondo, Y., Hu, M., Zhang, Y., Andreae,

893 M. O., and Poschl, U.: Cloud condensation nuclei in polluted air and biomass burning smoke near the
894 mega-city Guangzhou, China -Part 2: Size-resolved aerosol chemical composition, diurnal cycles, and
895 externally mixed weakly CCN-active soot particles, *Atmos. Chem. Phys.*, 11, 2817–2836,
896 <https://doi.org/10.5194/acp-11-2817-2011>, 2011.

897 Saha, P. K., Khlystov, A., and Grieshop, A. P.: Downwind evolution of the volatility and mixing
898 state of near-road aerosols near a US interstate highway, *Atmos. Chem. Phys.*, 18, 2139–2154,
899 <https://doi.org/10.5194/acp-18-2139-2018>, 2018.

900 Sedlacek, A. J., Lewis, E. R., Kleinman, L., Xu, J., and Zhang, Q.: Determination of and evidence
901 for non-core-shell structure of particles containing black carbon using the Single-Particle Soot
902 Photometer (SP2), *Geophysical Research Letters*, 39, L06802, <https://doi.org/10.1029/2012GL050905>,
903 2012.

904 Shi, J., Hong, J., Ma, N., Luo, Q., He, Y., Xu, H., Tan, H., Wang, Q., Tao, J., Zhou, Y., Han, S.,
905 Peng, L., Xie, L., Zhou, G., Xu, W., Sun, Y., Cheng, Y., and Su, H.: Measurement report: On the
906 difference in aerosol hygroscopicity between high and low relative humidity conditions in the North
907 China Plain, *Atmos. Chem. Phys.*, 22, 4599–4613, <https://doi.org/10.5194/acp-22-4599-2022>, 2022.

908 Stevens, R., Ryjkov, A., Majdzadeh, M., and Dastoor, A.: An improved representation of aerosol
909 mixing state for air quality–weather interactions, *Atmos. Chem. Phys.*, 22, 13527–13549,
910 <https://doi.org/10.5194/acp-22-13527-2022>, 2022.

911 Stolzenburg, M. R. and McMurry, P. H.: Equations governing single and tandem DMA
912 configurations and a new lognormal approximation to the transfer function, *Aerosol Science and
913 Technology*, 42, 421–432, 2008.

914 Su, H., Rose, D., Cheng, Y. F., Gunthe, S. S., Massling, A., Stock, M., Wiedensohler, A., Andreae,
915 M. O., and Poschl, U.: Hygroscopicity distribution concept for measurement data analysis and
916 modeling of aerosol particle mixing state with regard to hygroscopic growth and CCN activation,
917 *Atmos. Chem. Phys.*, 10, 7489–7503, <https://doi.org/10.5194/acp-10-7489-2010>, 2010.

918 Subramanian, R., Kok, G. L., Baumgardner, D., Clarke, A., Shinozuka, Y., Campos, T. L., Heizer,
919 C. G., Stephens, B. B., de Foy, B., Voss, P. B., and Zaveri, R. A.: Black carbon over Mexico: the effect
920 of atmospheric transport on mixing state, mass absorption cross-section, and BC/CO ratios, *Atmos.
921 Chem. Phys.*, 10, 219–237, <https://doi.org/10.5194/acp-10-219-2010>, 2010.

922 Tan, H., Xu, H., Wan, Q., Li, F., Deng, X., Chan, P. W., Xia, D., and Yin, Y.: Design and
923 Application of an Unattended Multifunctional H-TDMA System, *Journal of Atmospheric and Oceanic
924 Technology*, 30, 1136–1148, <https://doi.org/10.1175/JTECH-D-12-00129.1>, 2013.

925 Tao, J., Zhao, C., Nan, M., and Ye, K.: Consistency and applicability of parameterization schemes
926 for the size-resolved aerosol activation ratio based on field measurements in the North China Plain,
927 *Atmospheric Environment*, 173, 316–324, 2018.

928 Tao, J., Kuang, Y., Ma, N., Zheng, Y., Wiedensohler, A., and Zhao, C.: An improved
929 parameterization scheme for size-resolved particle activation ratio and its application on comparison
930 study of particle hygroscopicity measurements between HTDMA and DMA-CCNC, *Atmospheric
931 Environment*, 226, 117403, <https://doi.org/10.1016/j.atmosenv.2020.117403>, 2020.

932 Tao, J., Kuang, Y., Ma, N., Hong, J., Sun, Y., Xu, W., Zhang, Y., He, Y., Luo, Q., Xie, L., Su,
933 H., and Cheng, Y.: Secondary aerosol formation alters CCN activity in the North China Plain, *Atmos.*
934 *Chem. Phys.*, 21, 7409–7427, <https://doi.org/10.5194/acp-21-7409-2021>, 2021.

935 Tao, M., Chen, L., Su, L., and Tao, J.: Satellite observation of regional haze pollution over the
936 North China Plain, *Journal of Geophysical Research: Atmospheres*, 117,
937 <https://doi.org/10.1029/2012JD017915>, 2012.

938 Thalman, R., de Sa, S. S., Palm, B. B., Barbosa, H. M. J., Poehlker, M. L., Alexander, M. L.,
939 Brito, J., Carbone, S., Castillo, P., Day, D. A., Kuang, C., Manzi, A., Ng, N. L., Sedlacek, A. J., Souza,
940 R., Springston, S., Watson, T., Poehlker, C., Poeschl, U., Andreae, M. O., Artaxo, P., Jimenez, J. L.,
941 Martin, S. T., and Wang, J.: CCN activity and organic hygroscopicity of aerosols downwind of an
942 urban region in central Amazonia: seasonal and diel variations and impact of anthropogenic emissions,
943 *Atmospheric Chemistry and Physics*, 17, 11779–11801, <https://doi.org/10.5194/acp-17-11779-2017>,
944 2017.

945 Ting, Y., Mitchell, E. J. S., Allan, J. D., Liu, D., Spracklen, D. V., Williams, A., Jones, J. M.,
946 Lea-Langton, A. R., McFiggans, G., and Coe, H.: Mixing State of Carbonaceous Aerosols of Primary
947 Emissions from “Improved” African Cookstoves, *Environ. Sci. Technol.*, 52, 10134–10143,
948 <https://doi.org/10.1021/acs.est.8b00456>, 2018.

949 Tomlin, J. M., Jankowski, K. A., Veghte, D. P., China, S., Wang, P., Fraund, M., Weis, J., Zheng,
950 G., Wang, Y., Rivera-Adorno, F., Raveh-Rubin, S., Knopf, D. A., Wang, J., Gilles, M. K., Moffet, R.
951 C., and Laskin, A.: Impact of dry intrusion events on the composition and mixing state of particles
952 during the winter Aerosol and Cloud Experiment in the Eastern North Atlantic (ACE-ENA), *Atmos.*
953 *Chem. Phys.*, 21, 18123–18146, <https://doi.org/10.5194/acp-21-18123-2021>, 2021.

954 Ulbrich, I. M., Canagaratna, M. R., Zhang, Q., Worsnop, D. R., and Jimenez, J. L.: Interpretation
955 of organic components from Positive Matrix Factorization of aerosol mass spectrometric data, *Atmos.*
956 *Chem. Phys.*, 9, 2891–2918, <https://doi.org/10.5194/acp-9-2891-2009>, 2009.

957 Wang, X., Ye, X., Chen, J., Wang, X., Yang, X., Fu, T.-M., Zhu, L., and Liu, C.: Direct links
958 between hygroscopicity and mixing state of ambient aerosols: estimating particle hygroscopicity from
959 their single-particle mass spectra, *Atmos. Chem. Phys.*, 20, 6273–6290, <https://doi.org/10.5194/acp-20-6273-2020>, 2020.

961 Wang, Y., Wang, X., Kondo, Y., Kajino, M., Munger, J. W., and Hao, J.: Black carbon and its
962 correlation with trace gases at a rural site in Beijing: Top-down constraints from ambient
963 measurements on bottom-up emissions, *Journal of Geophysical Research: Atmospheres*, 116,
964 <https://doi.org/10.1029/2011JD016575>, 2011.

965 Wang, Y., Zhang, F., Li, Z., Tan, H., Xu, H., Ren, J., Zhao, J., Du, W., and Sun, Y.: Enhanced
966 hydrophobicity and volatility of submicron aerosols under severe emission control conditions in
967 Beijing, *Atmos. Chem. Phys.*, 17, 5239–5251, <https://doi.org/10.5194/acp-17-5239-2017>, 2017.

968 Wang, Y., Hu, R., Wang, Q., Li, Z., Cribb, M., Sun, Y., Song, X., Shang, Y., Wu, Y., Huang, X.,
969 and Wang, Y.: Different effects of anthropogenic emissions and aging processes on the mixing state
970 of soot particles in the nucleation and accumulation modes, *Atmos. Chem. Phys.*, 22, 14133–14146,
971 <https://doi.org/10.5194/acp-22-14133-2022>, 2022.

972 Wehner, B., Berghof, M., Cheng, Y. F., Achtert, P., Birmili, W., Nowak, A., Wiedensohler, A.,
973 Garland, R. M., Pöschl, U., Hu, M., and Zhu, T.: Mixing state of nonvolatile aerosol particle fractions
974 and comparison with light absorption in the polluted Beijing region, *Journal of Geophysical Research:*
975 *Atmospheres*, 114, <https://doi.org/10.1029/2008JD010923>, 2009.

976 Wu, Y., Wang, X., Tao, J., Huang, R., Tian, P., Cao, J., Zhang, L., Ho, K.-F., Han, Z., and Zhang,
977 R.: Size distribution and source of black carbon aerosol in urban Beijing during winter haze episodes,
978 *Atmos. Chem. Phys.*, 17, 7965–7975, <https://doi.org/10.5194/acp-17-7965-2017>, 2017.

979 Xu, W., Sun, Y., Wang, Q., Zhao, J., Wang, J., Ge, X., Xie, C., Zhou, W., Du, W., Li, J., Fu, P.,
980 Wang, Z., Worsnop, D. R., and Coe, H.: Changes in Aerosol Chemistry From 2014 to 2016 in Winter
981 in Beijing: Insights From High-Resolution Aerosol Mass Spectrometry, *Journal of Geophysical*
982 *Research: Atmospheres*, 124, 1132–1147, <https://doi.org/10.1029/2018JD029245>, 2019.

983 Xu, W. Y., Zhao, C. S., Ran, L., Deng, Z. Z., Liu, P. F., Ma, N., Lin, W. L., Xu, X. B., Yan, P.,
984 He, X., Yu, J., Liang, W. D., and Chen, L. L.: Characteristics of pollutants and their correlation to
985 meteorological conditions at a suburban site in the North China Plain, *Atmos. Chem. Phys.*, 11, 4353–
986 4369, <https://doi.org/10.5194/acp-11-4353-2011>, 2011.

987 Yang, Z., Ma, N., Wang, Q., Li, G., Pan, X., Dong, W., Zhu, S., Zhang, S., Gao, W., He, Y., Xie,
988 L., Zhang, Y., Kuhn, U., Xu, W., Kuang, Y., Tao, J., Hong, J., Zhou, G., Sun, Y., Su, H., and Cheng,
989 Y.: Characteristics and source apportionment of black carbon aerosol in the North China Plain,
990 *Atmospheric Research*, 276, 106246, <https://doi.org/10.1016/j.atmosres.2022.106246>, 2022.

991 Zhang, F., Li, Y., Li, Z., Sun, L., Li, R., Zhao, C., Wang, P., Sun, Y., Liu, X., Li, J., Li, P., Ren,
992 G., and Fan, T.: Aerosol hygroscopicity and cloud condensation nuclei activity during the AC3Exp
993 campaign: implications for cloud condensation nuclei parameterization, *Atmos. Chem. Phys.*, 14,
994 13423–13437, <https://doi.org/10.5194/acp-14-13423-2014>, 2014.

995 Zhang, S., Shen, X., Sun, J., Zhang, Y., Zhang, X., Xia, C., Hu, X., Zhong, J., Wang, J., and Liu,
996 S.: Atmospheric Particle Hygroscopicity and the Influence by Oxidation State of Organic Aerosols in
997 Urban Beijing, *Journal of Environmental Sciences*, 124, 544–556,
998 <https://doi.org/10.1016/j.jes.2021.11.019>, 2023.

999 Zhang, S. L., Ma, N., Kecorius, S., Wang, P. C., Hu, M., Wang, Z. B., Größ, J., Wu, Z. J., and
1000 Wiedensohler, A.: Mixing state of atmospheric particles over the North China Plain, *Atmospheric*
1001 *Environment*, 125, 152–164, 2016.

1002 Zhang, Y., Su, H., Ma, N., Li, G., Kecorius, S., Wang, Z., Hu, M., Zhu, T., He, K., Wiedensohler,
1003 A., Zhang, Q., and Cheng, Y.: Sizing of Ambient Particles From a Single-Particle Soot Photometer
1004 Measurement to Retrieve Mixing State of Black Carbon at a Regional Site of the North China Plain,
1005 *Journal of Geophysical Research: Atmospheres*, 123, 12,778–12,795,
1006 <https://doi.org/10.1029/2018JD028810>, 2018.

1007 Zhao, G., Tao, J., Kuang, Y., Shen, C., Yu, Y., and Zhao, C.: Role of black carbon mass size
1008 distribution in the direct aerosol radiative forcing, *Atmos. Chem. Phys.*, 19, 13175–13188,
1009 <https://doi.org/10.5194/acp-19-13175-2019>, 2019.

1010 Zhao, G., Tan, T., Hu, S., Du, Z., Shang, D., Wu, Z., Guo, S., Zheng, J., Zhu, W., Li, M., Zeng,
1011 L., and Hu, M.: Mixing state of black carbon at different atmospheres in north and southwest China,
1012 *Atmos. Chem. Phys.*, 22, 10861–10873, <https://doi.org/10.5194/acp-22-10861-2022>, 2022.

1013 Zheng, H., Kong, S., Wu, F., Cheng, Y., Niu, Z., Zheng, S., Yang, G., Yao, L., Yan, Q., Wu, J.,
1014 Zheng, M., Chen, N., Xu, K., Yan, Y., Liu, D., Zhao, D., Zhao, T., Bai, Y., Li, S., and Qi, S.: Intra-
1015 regional transport of black carbon between the south edge of the North China Plain and central China
1016 during winter haze episodes, *Atmos. Chem. Phys.*, 19, 4499–4516, [https://doi.org/10.5194/acp-19-](https://doi.org/10.5194/acp-19-4499-2019)
1017 [4499-2019](https://doi.org/10.5194/acp-19-4499-2019), 2019.

1018 Zhuang, B. L., Li, S., Wang, T. J., Deng, J. J., Xie, M., Yin, C. Q., and Zhu, J. L.: Direct radiative
1019 forcing and climate effects of anthropogenic aerosols with different mixing states over China,
1020 *Atmospheric Environment*, 79, 349–361, <https://doi.org/10.1016/j.atmosenv.2013.07.004>, 2013.

Table 1. Definitions and descriptions of abbreviations.

Abbreviation	Full name and/or Definition
	Biomass Burning Organic Aerosol
BBOA	Characterized by obvious m/z 60 (mainly C ₂ H ₄ O ₂ ⁺) and 73 (mainly C ₃ H ₅ O ₂ ⁺), which are two indicators of biomass burning
	Fossil Fuel Organic Aerosol
FFOA	A mixed factor that comprises traffic emissions and coal combustion, which was characterized by typical hydrocarbon ion series
	Oxygenated Organic Aerosol
OOA1 and OOA2	Two OOA factors resolved from the PMF analysis
	Secondary Organic Aerosol
SOA	Summation of OOA1 and OOA2
	Primary Organic Aerosol
POA	Summation of BBOA and FFOA
	Secondary Inorganic Aerosols, including nitrate, sulfate, and ammonium
SIA	Secondary Inorganic Aerosols, including nitrate, sulfate, and ammonium
PM _{2.5}	Particulate Matter with an aerodynamic diameter <2.5 μm
PM ₁	Particulate Matter with an aerodynamic diameter <1 μm
NR-PM ₁	Non-refractory PM ₁
MF	Mass Fraction
<i>D_p</i>	Particle diameter after humidification or heating
<i>D_d</i>	Particle diameter under dry conditions without humidification or heating
κ	Hygroscopicity parameter
SS	Supersaturation
SPAR	Size-resolved Particle Activation Ratio

Size-dependent CCN activity under a specific SS

Maximum Activation Fraction

MAF An asymptote of the measured SPAR curve at large particle sizes and represents the number fraction of CCNs to total particles

Midpoint activation diameter

D_a Linked to the hygroscopicity of CCNs

Growth factor

GF The ratio between particles with and without humidification and is linked to aerosol hygroscopicity

Shrinkage Factor

SF The ratio between particles with and without heating and is linked to aerosol volatility

Probability Distribution Function

PDF

Number Fraction of Hydrophilic aerosol whose hygroscopicity parameter is $> \sim 0.07$

NF_H

Number Fraction of Volatile aerosol whose Shrinkage Factor at 200 °C is < 0.85

NF_V

Number Fraction of black carbon (BC)-free particles

NF_{noBC}

Number Fraction of thickly coated BC particles

NF_{CBC}

The number concentration ratio of externally mixed BC particles in total BC-containing particles

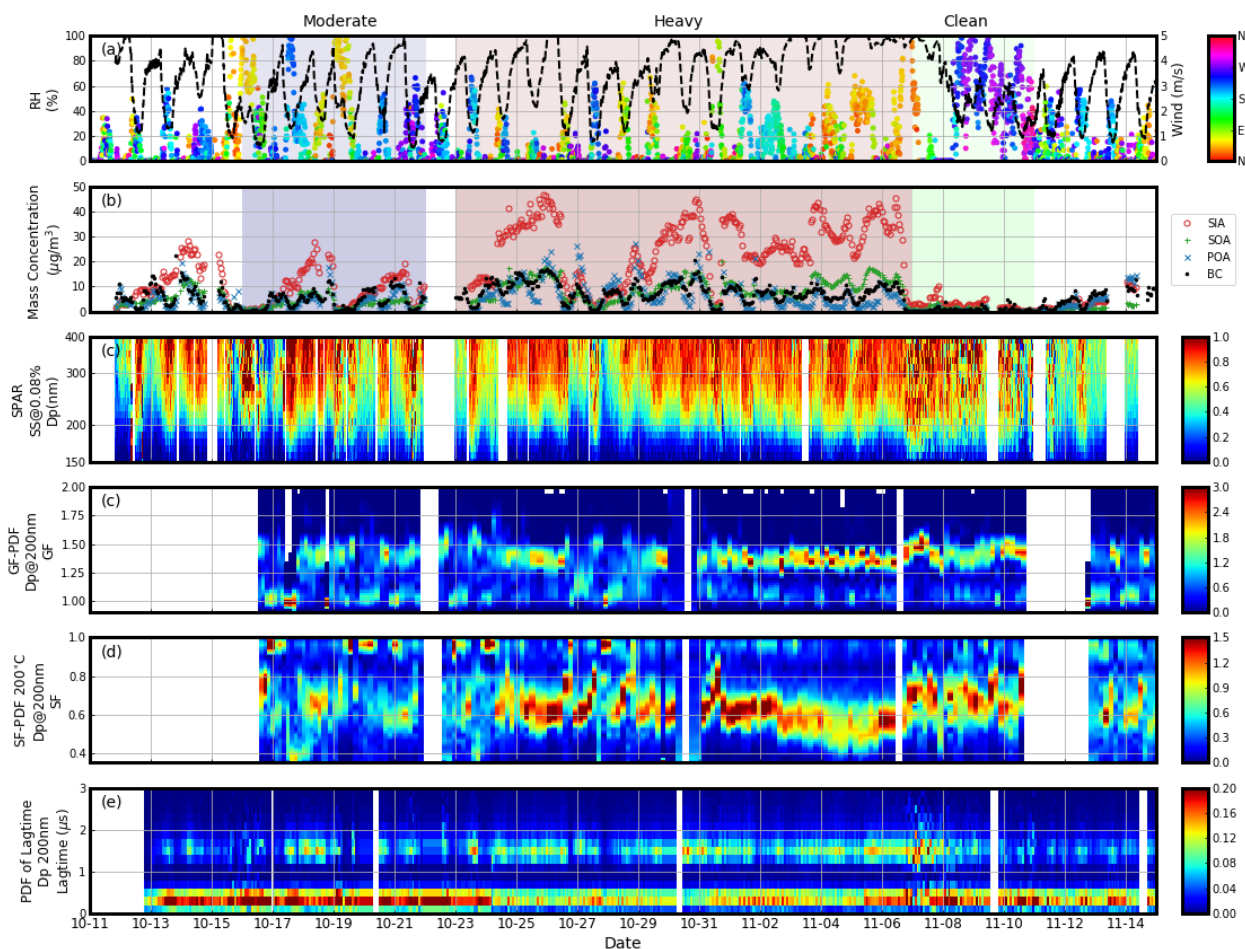
R_{exBC}

Externally mixed BC particles are defined as identified bare/thinly coated BC-containing particles

NF_A-NF_B

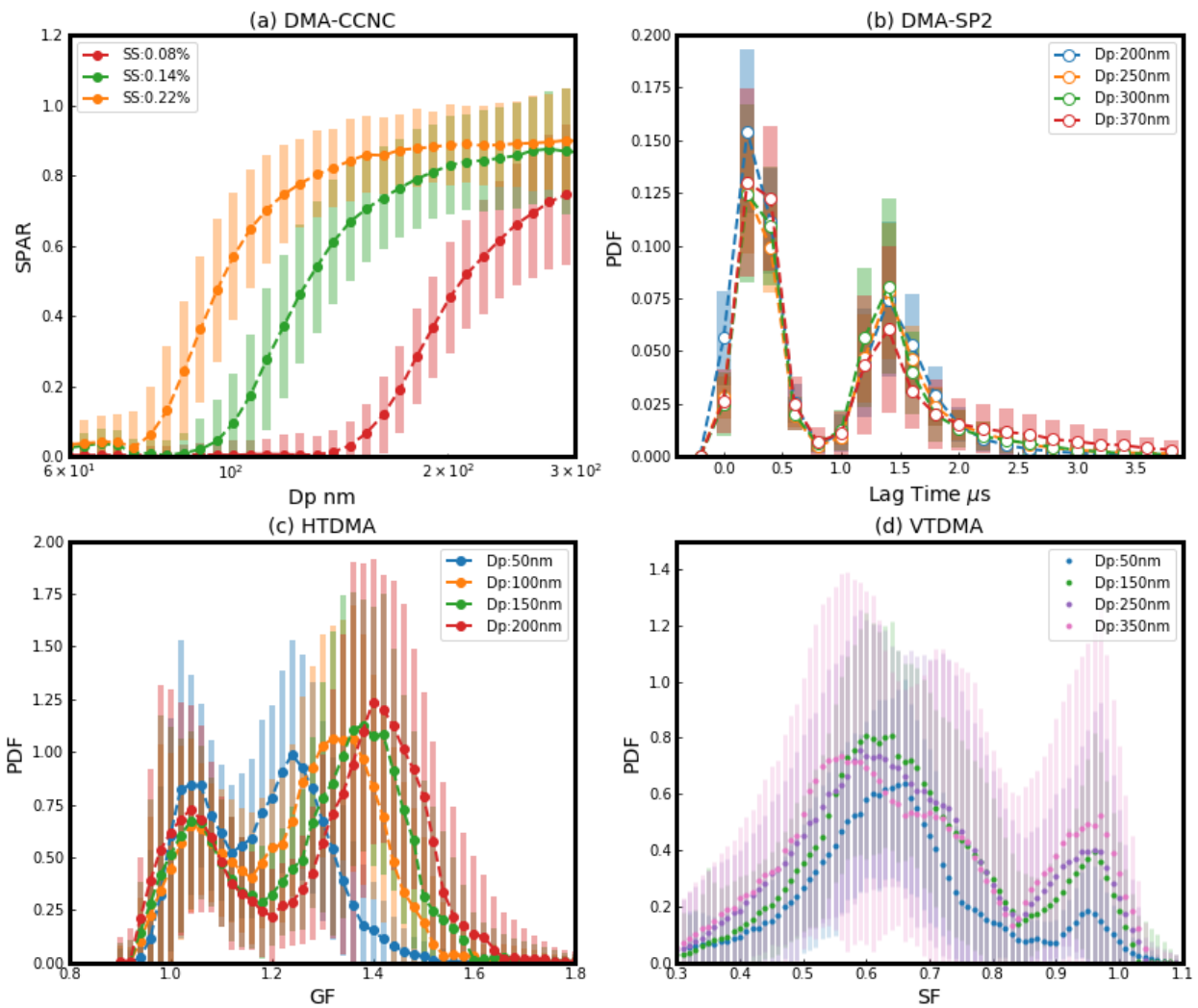
(NF_{noBC}-NF_H, NF_V-NF_H, NF_{noBC}-NF_V, NF_V-MAF, NF_{noBC}-MAF)

The difference between the number fraction of A and B



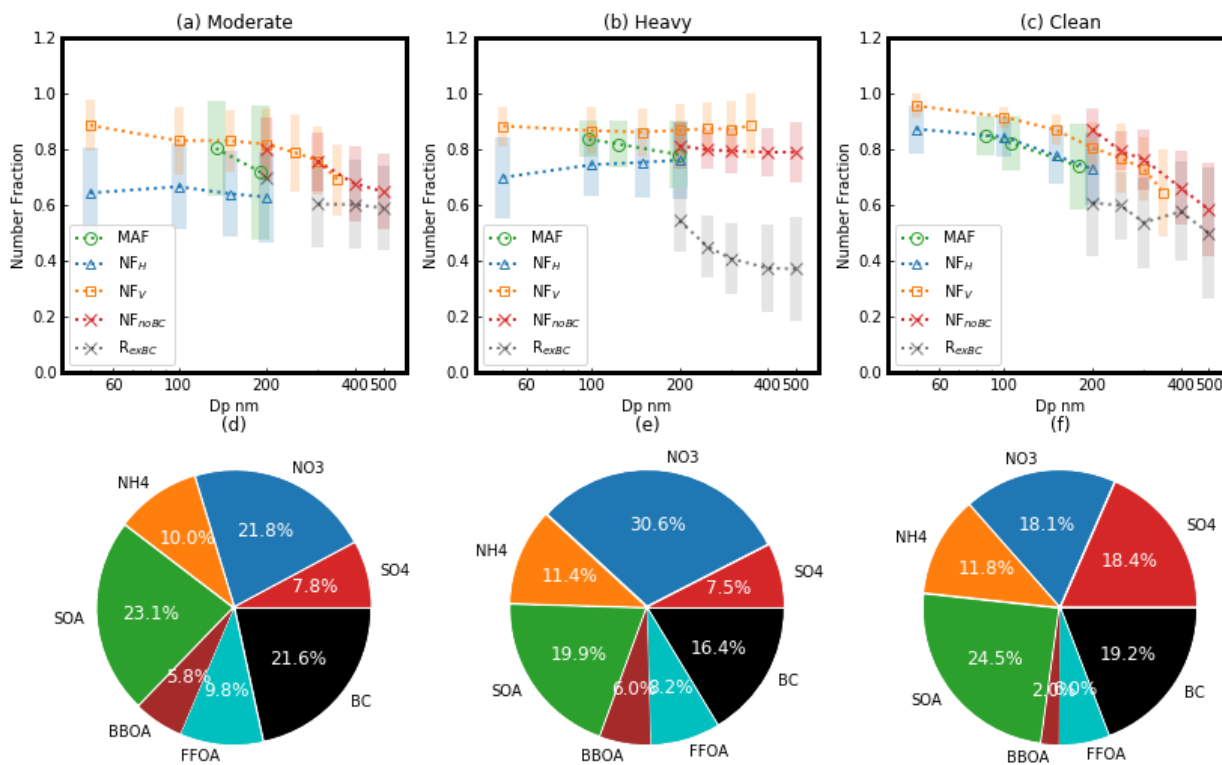
1023

1024 **Figure 1.** Overview of the measurements during the campaign: **(a)** meteorological parameters: wind speed (dots) and
 1025 relative humidity (RH) (black line), with colors of dots representing wind direction; **(b)** mass concentrations of
 1026 aerosol chemical compositions: secondary inorganic aerosols (SIA, red circle), secondary organic aerosols (SOA,
 1027 green plus), primary organic aerosols (POA, blue x) and black carbon (BC, black dots); **(c)** Size-resolved Particle
 1028 Activation Ratio (SPAR) under supersaturation (SS) of 0.08% observed by the DMA-CCNC, with warmer colors
 1029 corresponding to higher values; **(d)** Probability Density Function (PDF) of growth factor (GF-PDF) at 200 nm
 1030 observed by the HTDMA; **(e)** PDF of shrinkage factor (SF-PDF) at 200 nm and 200 °C observed by the VTDMA;
 1031 **(f)** PDF of lag time at 200 nm observed by the DMA-SP2. The blue, red, and green shaded periods represent the three
 1032 periods with moderate pollution, heavy pollution, and clean conditions, respectively.



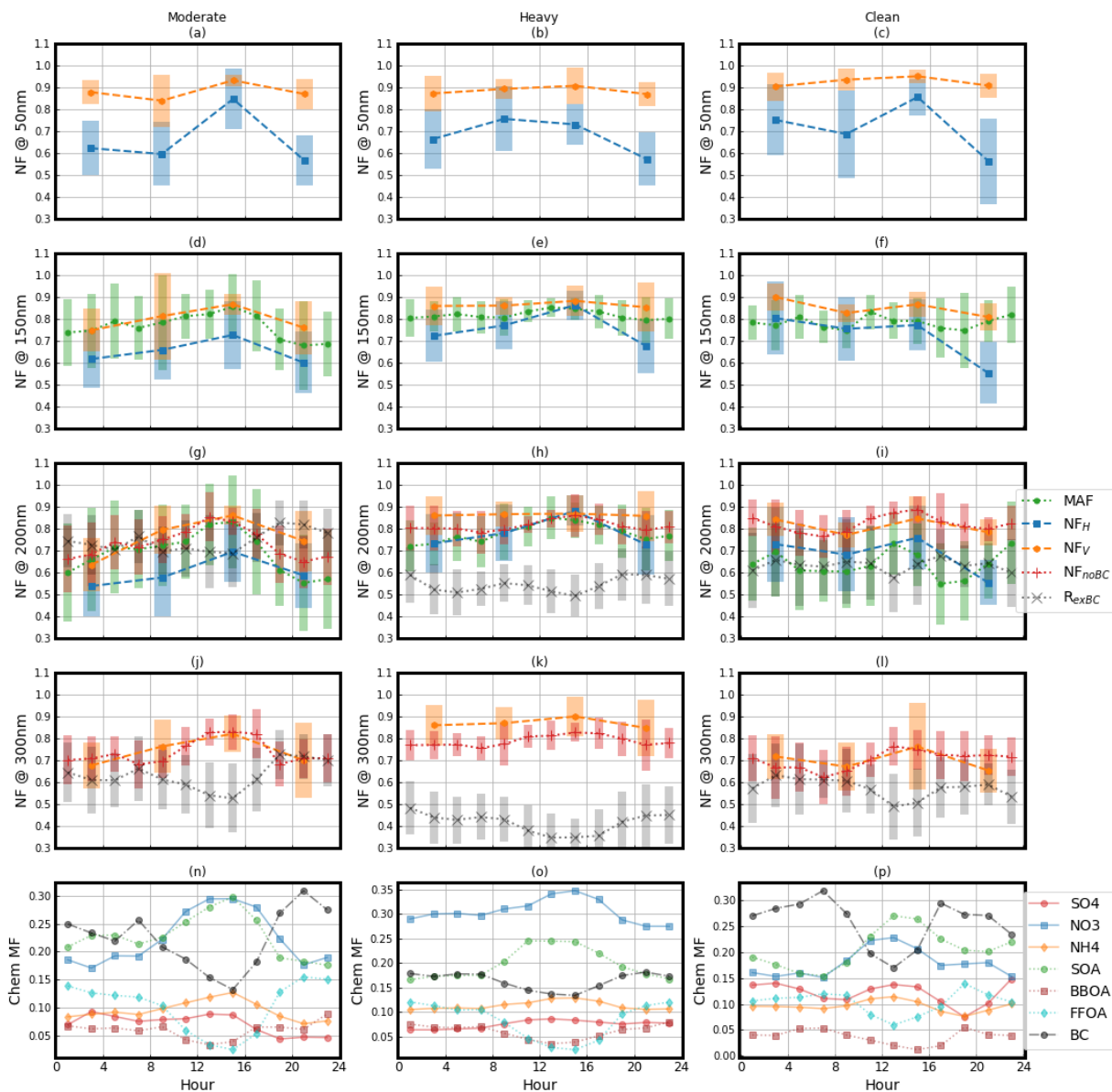
1033

1034 **Figure 2.** The campaign average of **(a)** Size-resolved Particle Activation Ratio (SPAR) curves measured by DMA-
 1035 CCNC at the three supersaturations (SSs, represented by different colors and markers), **(b)** Probability Density
 1036 Function (PDF) of lag time measured by DMA-SP2 at four particle sizes (represented by different colors and markers),
 1037 **(c)** PDF of growth factor (GF) measured by HTDMA at four particle sizes (represented by different colors and
 1038 markers), **(d)** PDF of shrinkage factor (SF) measured by VTDMA under the temperature of 200 °C at five particle
 1039 sizes (represented by different colors and markers). The shaded areas indicate the standard deviations.



1040

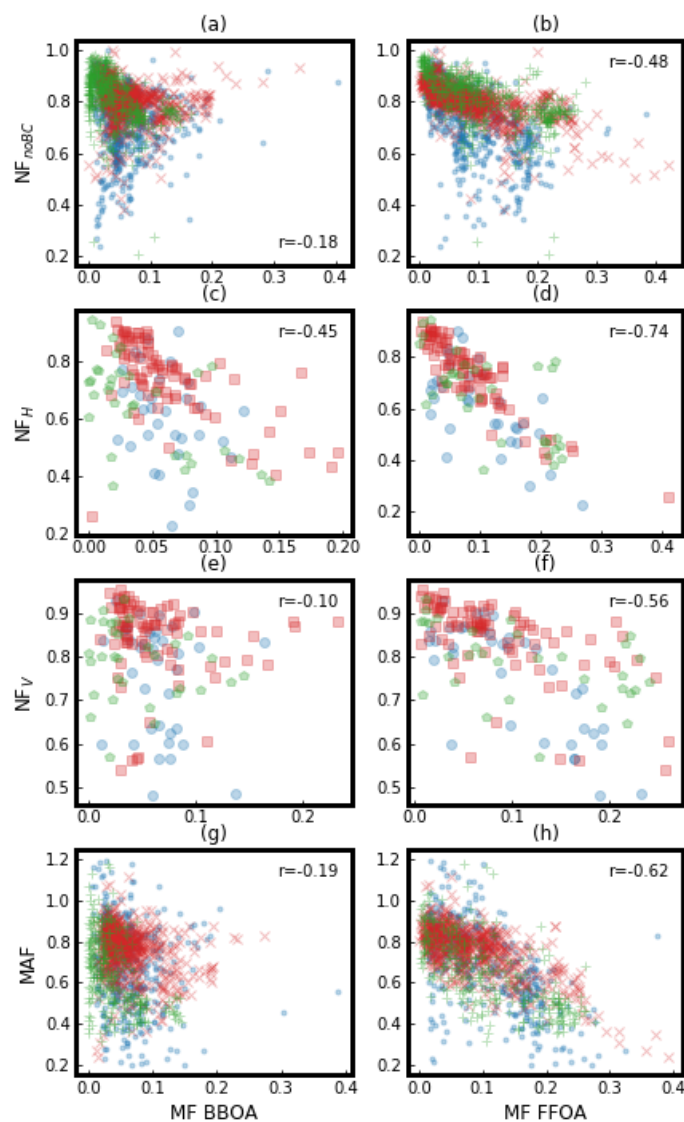
1041 **Figure 3.** (a–c) Size dependence of MAF (green circle), NF_H (blue triangle), NF_V (yellow square), NF_{noBC} (red x),
 1042 and R_{exBC} (black x) during the three periods. **MAF**: Maximum Activation Fraction, an asymptote of the measured
 1043 Size-resolved Particle Activation Ratio (SPAR) curve at large particle. **NF_H** : Number Fraction of Hydrophilic aerosol
 1044 whose hygroscopicity parameter is higher than ~ 0.07 . **NF_V** : Number Fraction of Volatile aerosol whose Shrink Factor
 1045 at $200\text{ }^\circ\text{C}$ is lower than 0.85. **NF_{noBC}** : Number Fraction of black carbon (BC)-free particles. **R_{exBC}** : Number fraction
 1046 of externally mixed BC particles in total BC-containing particles. (d–f) Corresponding mass fractions (MFs) of
 1047 aerosol chemical compositions (identified by colors) during the three periods, including secondary organic aerosols
 1048 (SOA), biomass burning organic aerosol (BBOA), fossil fuel organic aerosols (FFOA), and inorganic ions including
 1049 sulfate (SO_4), nitrate (NO_3), and ammonium (NH_4).



1050

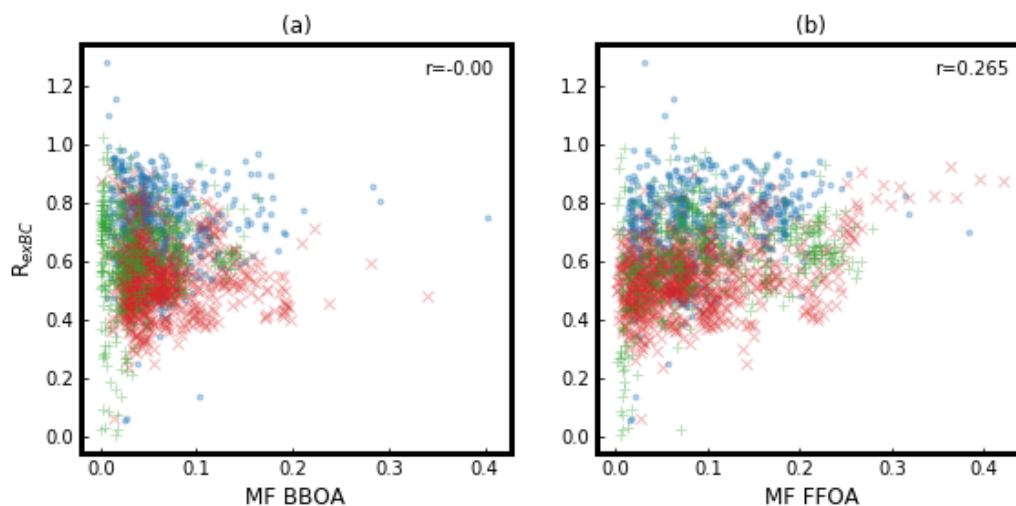
1051 **Figure 4. (a–l)** Diurnal variations of aerosol mixing state parameters (identified by color and marker) at different
 1052 particle sizes (50, 150, 200, and 300 nm) during the three periods. The shaded areas indicate the standard deviations.
 1053 **(m–o)** Diurnal variations of mass fractions (MFs) of aerosol chemical compositions, including secondary organic
 1054 aerosols (SOA), biomass burning organic aerosol (BBOA), fossil fuel organic aerosols (FFOA), and inorganic ions
 1055 including sulfate (SO_4), nitrate (NO_3), and ammonium (NH_4) (identified by color and marker) during the three periods.

1056



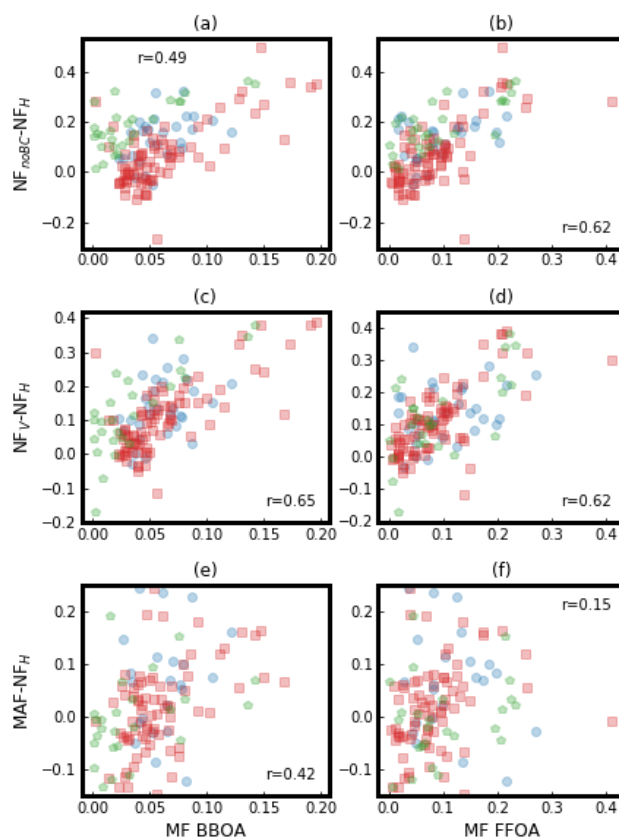
1057

1058 **Figure 5.** The correlations between aerosol mixing state parameters and mass fractions (MFs) of biomass burning
 1059 organic aerosol (BBOA) and fossil fuel organic aerosols (FFOA) during different periods (moderately polluted period:
 1060 blue dot or circle; heavily polluted period: red x or square; clean period: green plus or pentagon), with r representing
 1061 the correlation coefficient.



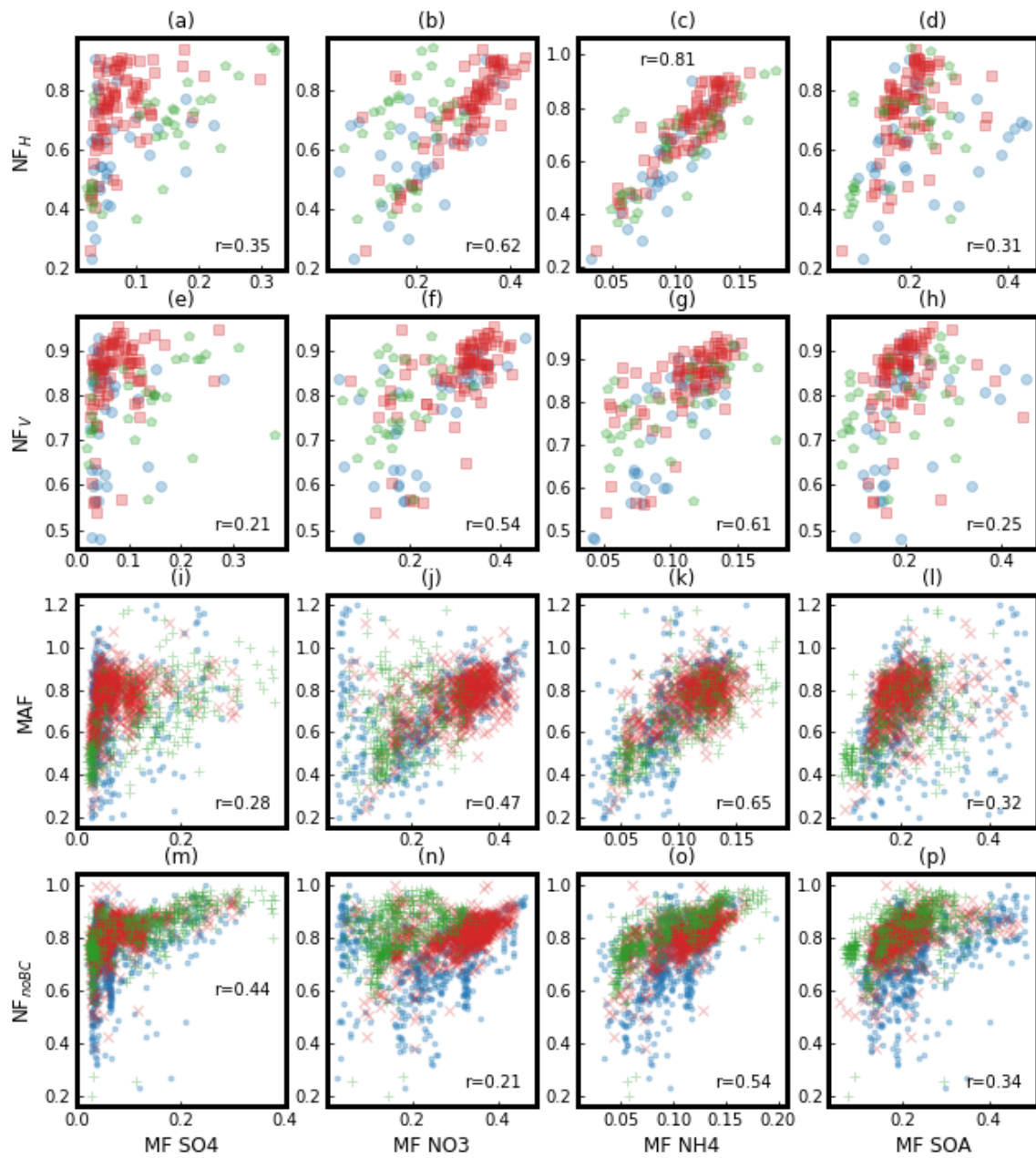
1062

1063 **Figure 6.** The correlations between the ratio of externally mixed black carbon (BC) in total BC particles (R_{exBC}) and
 1064 mass fractions (MFs) of biomass-burning organic aerosol (**BBOA**) and fossil fuel organic aerosols (**FFOA**) during
 1065 different periods (moderately polluted period: blue dot; heavily polluted period: red x; clean period: green plus), with
 1066 r representing correlation coefficient.



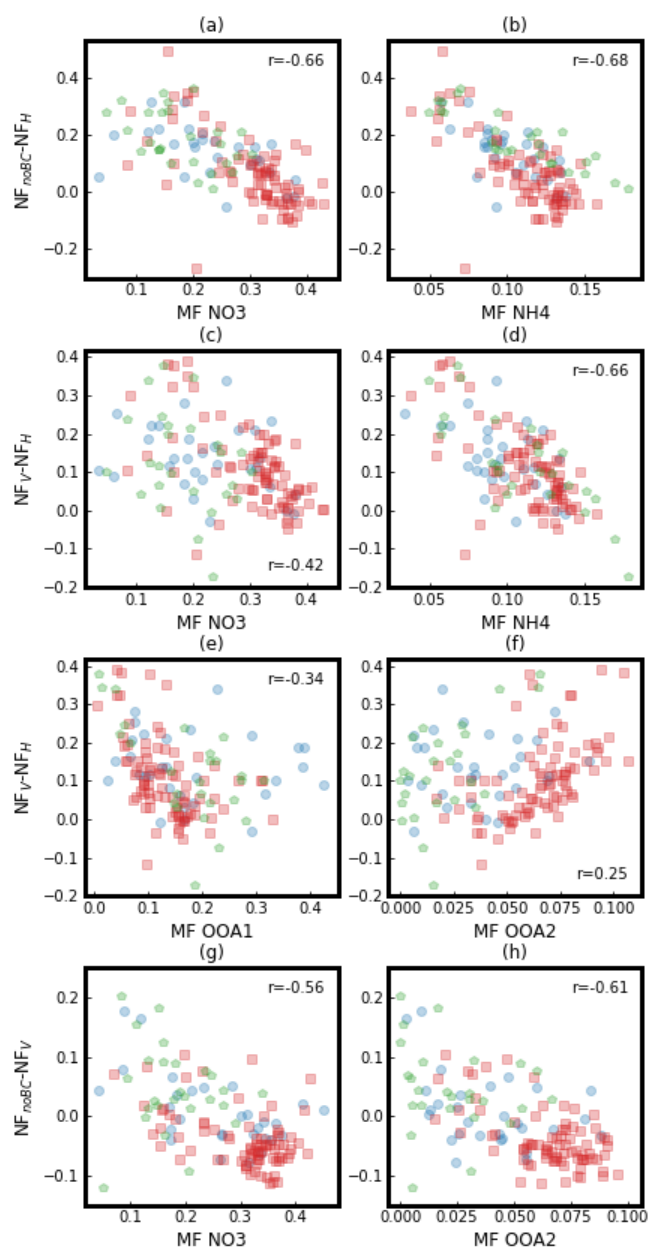
1067

1068 **Figure 7.** The correlations between the difference among the four aerosol mixing state parameters at particle size 200
 1069 nm and mass fractions (MFs) of biomass burning organic aerosol (**BBOA**) and fossil fuel organic aerosols (**FFOA**)
 1070 during different periods (moderately polluted period: blue circle; heavily polluted period: red square; clean period:
 1071 green pentagon), with r representing correlation coefficient.



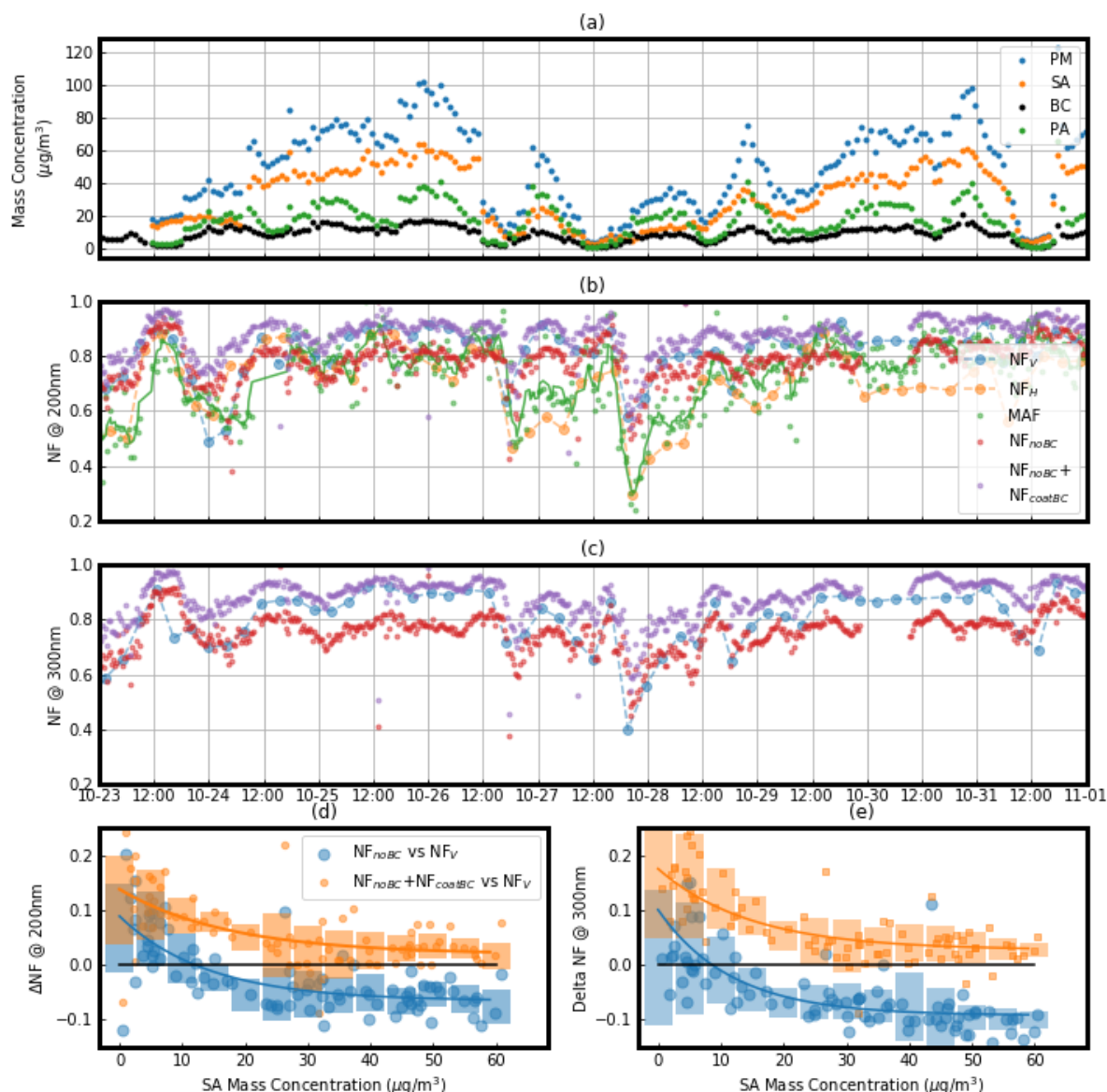
1072

1073 **Figure 8.** The correlation between the four aerosol mixing state parameters and mass fraction (MF) of secondary
 1074 aerosol (SA) components during different periods (moderately polluted period: blue dot or circle; heavily polluted
 1075 period: red x or square; clean period: green plus or pentagon), with r representing correlation coefficient. SA
 1076 components include secondary organic aerosols (SOA), sulfate (SO₄), nitrate (NO₃), and ammonium (NH₄)



1077

1078 **Figure 9.** The correlation between the difference among the four aerosol mixing state parameters and mass fraction
 1079 (MF) of secondary aerosol (SA) chemical components during different periods. OOA1 and OOA2 are two secondary
 1080 organic aerosol (SOA) factors resolved from aerosol mass spectrometer (AMS) measurements using the Positive
 1081 Matrix Factorization (PMF) technique. Moderately polluted period: blue circle; heavily polluted period: red square;
 1082 clean period: green pentagon.



1083

1084 **Figure 10.** Variations of different aerosol mixing state parameters during the pollution accumulation process. **(a)** The
 1085 time series of mass concentrations of non-refractory PM_{10} (NR- PM_{10}), secondary aerosols (SAs) (including inorganic
 1086 ions and secondary organic aerosols (SOA)), primary organic aerosols (POA) and black carbon (BC) (identified by
 1087 colors and markers). **(b and c)** The variations of different aerosol mixing state parameters (identified by colors and
 1088 markers) at particle size 200 nm **(b)** and 300 nm **(c)**. **(d and e)** The variations of the difference between NF_V and
 1089 NF_{noBC} ($\text{NF}_V - \text{NF}_{noBC}$, blue large circle) and the difference between NF_V and $\text{NF}_{noBC} + \text{NF}_{coatedBC}$ ($\text{NF}_V - (\text{NF}_{noBC} + \text{NF}_{coatedBC})$,
 1090 yellow small circle) with the mass concentration of SA at particle size 200 nm **(d)** and 300 nm **(e)** $\text{NF}_{coatedBC}$: Number
 1091 Fraction of thickly coated black carbon (BC) particles.